Chaotic advection in a two-dimensional perturbed shear-vortex flow

Kunnen, R.P.J.

Award date:
2004

TU/e technische universiteit eindhoven
Eindhoven University of Technology

Department of Applied Physics
Fluid Dynamics Laboratory
Building: Cascade
P.O. Box 513
5600 MB Eindhoven

Title: **Chaotic advection in a two-dimensional perturbed shear-vortex flow**

Author: R.P.J. Kunnen

Report number: R-1635-A

Date: May 2004

Group : Vortex Dynamics, Department of Applied Physics,
Eindhoven University of Technology, The Netherlands

Advisors : prof. dr. ir. G.J.F. van Heijst (TU/e)
dr. ir. R.R. Trieling (TU/e)
dr. ir. L.P.J. Kamp (TU/e)

Abstract

A two-dimensional incompressible flow can be described as a Hamiltonian system, with the stream function playing the role of the Hamiltonian function. It is known that two-dimensional flows with a time-periodic stream function can produce chaotic particle paths. In the flow field associated with a vortex in a linear shear with a time-dependent perturbation the chaotic particle paths enable complicated mixing and transport of fluid. This flow is investigated in several ways.

The fluid exchange mechanism has been described by use of lobe dynamics. The lobes are defined by the stable and unstable manifolds in a Poincaré section. A contour kinematics simulation provided these manifolds. The amount of fluid exchange was also calculated with the analytical Melnikov theory, with remarkable agreement.

The chaotic behaviour of the flow was indicated by monitoring the deformation and length stretch of passive contours in a contour kinematics simulation. Exponential stretch is an indication of chaotic mixing.

Another type of numerical simulations involved a large number of passive tracers that were advected with the flow. From these simulations the region where mixing takes place can be defined, along with information on the residence time of tracers in this mixing region.

In laboratory experiments on a turntable the unstable manifolds were visualised with dye. An associated contour kinematics simulation showed a striking resemblance. Particle tracking experiments were performed to confirm the validity of the linearity and the harmonic time dependence of the shear. From a particle tracking experiment on a vortex in perturbed shear the vorticity distribution was calculated, showing the advection of vorticity via the lobes.

Contents

Chapter 1

Introduction

Geophysical flows are to a good approximation two-dimensional. These flows tend to behave as though they were two-dimensional due to one (or more) of the following three ingredients.

Geometrical confinement of the flow can cause two-dimensional behaviour. A striking example is the flow in thin soap films, as studied by Couder & Basdevant (1986). A similar confinement is present in atmospheric flows, where the typical horizontal dimensions (order 1000 km) are much larger than the vertical dimensions (order 1 km). Shallow fluid layers also exhibit two-dimensional behaviour.

If the fluid has a density stratification the motion is also confined to two dimensions. Fluid elements of a certain density are confined to a layer of fluid of the same density by gravity. The most important example is the flow in oceans, in which salinity gradients exist. Many experiments on vortices in salinity stratified fluids have been performed, see *e.g.* Flór & van Heijst (1996).

A third method of obtaining a two-dimensional flow is by applying a background rotation. Under certain conditions the rotation causes the flow to behave as a two-dimensional flow, by virtue of the Taylor-Proudman theorem. This method is used in the laboratory experiments in this work. Many earlier studies used this method, see *e.g.* Hopfinger & van Heijst (1993).

Two-dimensional flows are characterised by the spontaneous emergence of coherent vortices, a process generally called 'self-organisation'. Energy initially distributed over both larger and smaller length scales is eventually concentrated in larger vortex structures. This is opposite to what happens in three-dimensional flows, where energy cascades down to smaller and smaller length scales until it is dissipated by viscous diffusion at the smallest scales.

The ordering of two-dimensional turbulence is nicely demonstrated in some numerical simulations. An example can be found in Legras *et al.* (1988). This work shows the emergence of several coherent vortex structures: monopoles, dipoles and tripoles. These structures are characterised by compact, coherent patches of vorticity, with one, two and three separate parts with closed streamlines, respectively. They remain close together since adjacent parts have vorticity of opposite sign. These vortex structures are also found in

laboratory experiments.

A monopolar vortex is composed of a single set of closed streamlines. Fluid moves along these streamlines around a central point. The flow due to the presence of vortices is thus observed as a position-dependent velocity field. As a first-order approximation the flow associated with the neighbouring vortices can be represented by a strain flow. The behaviour of a vortex in a strain flow has been studied extensively, both numerically and experimentally, by Trieling *et al.* (1997) and Trieling & van Heijst (1998). The combined effect of strain and rotation is a linear shear flow. Moore & Saffman (1971) analytically considered steady elliptic vortices in a linear shear, later extended by Kida (1981) to include unsteady solutions.

The steady flow changes drastically if a time-dependent perturbation is introduced. Such a perturbed two-dimensional flow can produce chaotic particle paths, thereby allowing for complicated mixing processes. Although the motion is still fully deterministic, finding a description of the flow by monitoring the individual particle paths is impossible due to the complex geometry of these paths. It is more insightful to observe the global topology of the flow rather than the motion of individual particles. This analysis is done using lobe dynamics, an application of dynamical systems theory.

Several studies have been performed on perturbed two-dimensional flows. An extensive study on a point vortex dipole in an oscillating strain was performed by Rom-Kedar *et al.* (1990) (also described in Leonard *et al.* (1987), Rom-Kedar & Wiggins (1991) and Wiggins (1992)). The fluid exchange in topography-modulated vortices can also be described using dynamical systems theory. Such an analysis of the motion of a vortex dipole on a β-plane was made by Velasco Fuentes *et al.* (1995). Another study considered the dynamics of a tripole on a γ-plane (Velasco Fuentes *et al.* 1996).

An individual vortex in a two-dimensional turbulent flow experiences an unsteady background flow due to constant changes in the surrounding vorticity distribution. In order to examine the influence of such an unsteady flow on an individual vortex a simple model is presented: a point vortex is placed in a harmonically perturbed linear shear flow. Observation of the behaviour of this model system may lead to a better understanding of two-dimensional turbulence.

In the present study the mixing properties of the suggested model system are investigated, both analytically and numerically. Lobe dynamics is used to describe tracer transport. The analytical Melnikov theory is also used to predict the magnitude of fluid exchange between the interior of the vortex and the ambient flow. Numerical simulations are used to seek confirmation of the lobe dynamics analysis and to demonstrate the chaotic behaviour of the flow. Finally, with results from laboratory experiments additional proof of the validity of the lobe dynamics is presented. These results also validate the use of the point vortex as model vortex.

This report is organised as follows. In chapter 2 the relevant definitions of dynamical systems are presented, along with application to the Hamiltonian system of a point vortex in a perturbed linear shear. Lobe dynamics and Melnikov theory are also discussed. The methods used in the numerical simulations and the obtained results are presented in chapter 3. The results from contour kinematics simulations are used to apply lobe dynamics.

Fluid exchange is quantified using direct numerical integration and with the Melnikov function. The advection of large numbers of passive tracers is simulated in order to determine an escape time distribution. Chapter 4 contains a visualisation of the lobe structure from laboratory experiments, illustrating the fluid exchange. The final conclusions are drawn in chapter 5.

Chapter 2

Theory

This chapter is divided into two parts. In the first section relevant terminology from dynamical systems theory is presented, along with applications to fluid transport as explained by lobe dynamics. The application of Melnikov theory is also discussed. The second section on rotating fluids contains a description of relevant flow phenomena that occur in fluids under background rotation.

2.1 Transport in dynamical systems

2.1.1 Hamiltonian systems

The trajectory $(x(t), y(t))$ of a passively advected fluid particle in an incompressible two-dimensional flow can be described by the following equations:

$$\frac{dx}{dt} = \frac{\partial \Psi}{\partial y}, \quad \frac{dy}{dt} = -\frac{\partial \Psi}{\partial x}. \tag{2.1}$$

Such a system is called a Hamiltonian system, where the stream function Ψ plays the role of the Hamiltonian function. If the flow is independent of time, *i.e.* $\Psi = \Psi(x, y)$, then the Hamiltonian system (2.1) is said to have one degree of freedom. For a time-dependent flow ($\Psi = \Psi(x, y, t)$) the system has two degrees of freedom. For Ψ a periodic function of time t, the system has 'one and a half' degrees of freedom (Ottino 1989). There are major differences in particle motion between flows of various degrees of freedom. In a system of one degree of freedom, *i.e.* a steady two-dimensional flow, no chaotic particle paths can occur. Time-periodic flows, however, can produce chaotic particle paths (Aref 1984). The occurrence of such paths enables complicated mixing and transport of fluid.

2.1.2 Point vortex in a linear shear

Consider the following Hamiltonian system. A point vortex of strength γ is placed in a linear shear flow with shear strength α. The shear contributes to the velocity field as $u = \alpha y$, with u the velocity component in the x-direction. The point vortex contributes

to the velocity field as $v_\theta = \gamma/2\pi r$, where v_θ is the azimuthal velocity, and r is the distance to the point vortex. The stream function Ψ for this flow is

$$\Psi = \frac{1}{2}\alpha y^2 - \frac{\gamma}{4\pi}\ln(x^2+y^2) + c, \tag{2.2}$$

with c an arbitrary constant.
Two stagnation points $\mathbf{p}_+$ and $\mathbf{p}_-$ exist in this flow. At $\mathbf{p}_\pm : (x,y) = (0, \pm\sqrt{\gamma/2\pi\alpha}) = (0, \pm r_s)$ the velocity is zero. In polar coordinates, defined as $x = r\cos\theta$; $y = r\sin\theta$, the stream function is

$$\Psi = \frac{1}{2}\alpha r^2 \sin^2\theta - \frac{\gamma}{2\pi}\ln r + c. \tag{2.3}$$

The streamline pattern is shown in figure 2.1. The dotted streamlines divide the flow into five regions: one region with closed streamlines inside the streamlines Ψ_e and Ψ_w, and four regions with unbounded streamlines. No fluid transport is possible through these dotted streamlines; they are therefore known as separatrices.

It is convenient to make Ψ zero at the separatrices. Therefore c is chosen to be $\frac{\gamma}{4\pi}\ln(r_s^2)$. To make the stream function dimensionless, introduce $\xi = r/r_s$ in equation (2.3) and scale Ψ by a factor $\gamma/4\pi$. The result is

$$\Psi = \xi^2 \sin^2\theta - \ln\xi^2 - 1. \tag{2.4}$$

2.1.3 Dynamical systems

The behaviour of this Hamiltonian system changes drastically when a perturbation is introduced in the flow. In this work the perturbation is a small harmonic variation in the shear strength α

$$\alpha(t) = \alpha_0\left[1 + \epsilon\cos(\omega_s t)\right], \tag{2.5}$$

in which α_0 is the basic-state shear strength, ϵ is the amplitude of perturbation, and ω_s is the perturbation frequency. Individual particle paths, as can be derived from the stream function Ψ, become highly complex and are no longer suited to find a description of the flow. Instead, it is more convenient to observe the global topology of the flow. This analysis can be done by using definitions from dynamical systems theory, introduced below. The analysis follows Ottino (1988), and is also presented in Beckers (1993) and van Lipzig (1994).

The equation of motion for a particle at $\mathbf{x} = (x,y)$ in the Eulerian velocity field $\mathbf{v}(\mathbf{x},t)$ is

$$\frac{d\mathbf{x}}{dt} = \mathbf{v}(\mathbf{x},t). \tag{2.6}$$

Equation (2.6) is an example of a dynamical system. This system of differential equations can be solved given an initial condition $\mathbf{x} = \mathbf{X}$ at $t = 0$. The solution is denoted by $\mathbf{x} =$

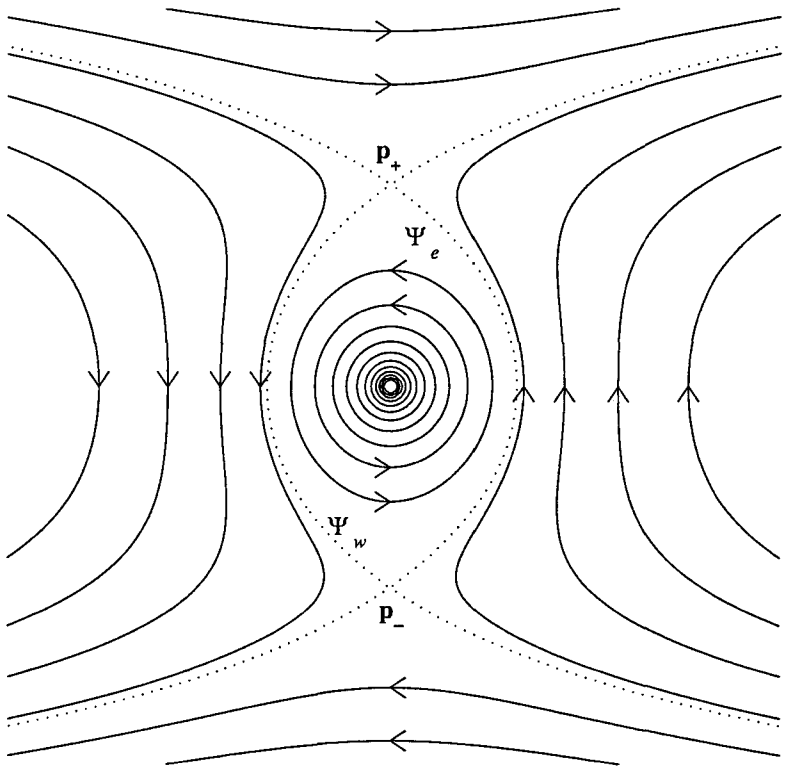

Figure 2.1: Streamlines of the point vortex in a linear shear flow. The separatrices are depicted by the dotted lines. They intersect at the stagnation points $\mathbf{p}_{\pm}$.

$\Phi_t(\mathbf{X})$, where $\Phi_t(\mathbf{X})$ gives the trajectory of a given particle with initial position $\mathbf{X}$ for all time t.

A special case occurs when $\mathbf{v}$ is time-periodic. In this case $\mathbf{v}(\mathbf{x},t) = \mathbf{v}(\mathbf{x},t+T)$, with T the period of $\mathbf{v}$. Although the system is fully deterministic the particle paths in the phase space $\mathbb{R}^2 \times \mathbb{R}$, with time t as third variable in addition to $\mathbf{x}$, can be highly complex. It is hard to obtain information about the system by monitoring lots of individual particle paths because of their complexity. It is more convenient to record the particle positions only at discrete times $t = 0, T, 2T, ...$ The position $\mathbf{x}_n$ of a particle after a time nT is given by $\mathbf{x}_n = \Phi_{nT}(\mathbf{x}_0)$, where $\mathbf{x}_0$ is its initial position. The continuous flow $\mathbf{x} = \Phi_t(\mathbf{X})$ can now be converted to a discrete mapping F:

$$\mathbf{x}_{n+1} = F(\mathbf{x}_n) = \Phi_T(\mathbf{x}_n). \tag{2.7}$$

This mapping, while far less complicated than the flow, still contains useful information on the flow. The subsequent mappings of the flow at times nT, with n integer, are also known as Poincaré sections. These Poincaré sections are a useful tool to study unsteady time-periodic flows since this technique tends to filter out redundant dynamical phenomena. Instead it reveals the underlying structures which govern various properties of the flow, such as mixing and transport.

In Hamiltonian systems the volume in phase space is a conserved quantity. Therefore the area is a conserved quantity in Poincaré maps. Thus a labelled patch can change shape after some iterations of the Poincaré map, yet its area does not change. A second property of the Poincaré map is orientation preservation. A line element $l(0)$, with points $\mathbf{p}_1(0), \mathbf{p}_2(0), ..., \mathbf{p}_m(0)$ on it in that order, will be mapped onto line element $l(n)$ after n iterations. The points $\mathbf{p}_1(n), \mathbf{p}_2(n), ..., \mathbf{p}_m(n)$ lie on $l(n)$ in the same order.

Usually, periodic points can be found on Poincaré sections. A point $\mathbf{P}$ is called a periodic point of period n of the mapping F if it returns to its original position after n iterations of the Poincaré map, *i.e.*

$$\mathbf{P} = F^n(\mathbf{P}). \tag{2.8}$$

Only periodic points of period 1 will be described. These points occur as fixed points on the Poincaré sections. There are three different types of periodic points: hyperbolic, elliptic, and parabolic. A circle of particles placed around a hyperbolic point will be stretched in one direction and contracted in another. A particle placed near an elliptic point will translate along a closed regular trajectory. See figure 2.2 for an example view of streamlines near such points. The parabolic point is untypical for the flows under study.

In the flow studied in this work the stagnation points $\mathbf{p}_\pm$ are hyperbolic points, while the centre of the vortex is an elliptic point. The streamline pattern in figure 2.1 also illustrates the hyperbolic or elliptic behaviour of the fixed points.

Each hyperbolic point $\mathbf{p}$ has two associated manifolds, the stable manifold $W^s(\mathbf{p})$ and the unstable manifold $W^u(\mathbf{p})$. These manifolds are defined as

$$\begin{aligned} W^s(\mathbf{p}) &= \{\forall\, \mathbf{X} \in \mathbb{R}^N | F(\mathbf{X}) \to \mathbf{p} \text{ as } t \to \infty\}, \\ W^u(\mathbf{p}) &= \{\forall\, \mathbf{X} \in \mathbb{R}^N | F(\mathbf{X}) \to \mathbf{p} \text{ as } t \to -\infty\}. \end{aligned} \tag{2.9}$$

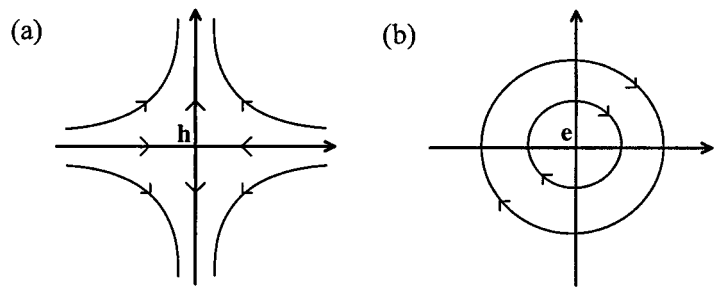

Figure 2.2: Illustration of the flow near (a) a hyperbolic point **h** *and (b) an elliptic point* **e**.

Particles near a hyperbolic point will be mapped onto the stable manifold as $t \to -\infty$. Similarly, they will be mapped onto the unstable manifold as $t \to \infty$. For the hyperbolic point as depicted in figure 2.2a, the y-axis is the unstable manifold and the x-axis is the stable manifold. In physical terms this implies that fluid is transported towards the hyperbolic point along the x-axis (stable manifold). The fluid is then transported away from the hyperbolic point along the y-axis (unstable manifold).

This provides a method for constructing the manifolds numerically (Ottino 1989). A large number of particles is placed in a circle around a hyperbolic point. Then the associated advection equations are integrated, and the positions of the particles are monitored at times nT. For n positive and increasing the unstable manifold is obtained; for n negative and decreasing the stable manifold is obtained.

It is possible to apply the terminology of dynamical systems to the flow due to a point vortex in a linear shear, depicted in figure 2.1. The stagnation points $\mathbf{p}_\pm$ are hyperbolic points. The location of the point vortex is an elliptic point. With the manifold definitions in equation (2.9) it can be concluded that the streamline Ψ_e is the stable manifold of $\mathbf{p}_+$ and the unstable manifold of $\mathbf{p}_-$. Consequently, the streamline Ψ_w is the stable manifold of $\mathbf{p}_-$ and the unstable manifold of $\mathbf{p}_+$.

Due to symmetry, mirroring the unstable manifold of $\mathbf{p}_+$ in the vertical axis yields the stable manifold of $\mathbf{p}_+$. Mirroring both the stable and unstable manifolds of $\mathbf{p}_+$ in the horizontal axis gives the unstable and stable manifolds of $\mathbf{p}_-$, respectively.

2.1.4 Lobe dynamics

For time-periodic perturbations the hyperbolic points $\mathbf{p}_\pm$ remain fixed points of the Poincaré map. However, the introduction of this perturbation has a profound effect on the shapes of the manifolds. The stable and unstable manifolds of the different hyperbolic points no longer coincide. Instead they intersect in a countable number of discrete points. These points are called heteroclinic points, since they are intersections of the stable and unstable manifolds of two different hyperbolic points. Intersections of the stable and unstable manifolds of the same hyperbolic point are known as homoclinic points.

The structure which results from the intersection of the manifolds of two different hyperbolic points is called a heteroclinic tangle. Part of the heteroclinic tangle of the flow

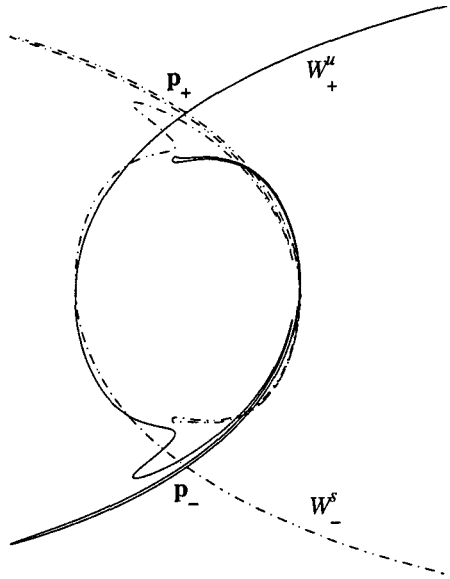

Figure 2.3: Part of the heteroclinic tangle of the flow under study. The solid line represents the unstable manifold of $\mathbf{p}_+$*. The dash-dotted line represents the stable manifold of* $\mathbf{p}_-$*. The other manifolds are left out for clarity.*

under study is shown in figure 2.3. For clarity, only the stable manifold of $\mathbf{p}_-$ and the unstable manifold of $\mathbf{p}_+$ are depicted. For the full heteroclinic tangle, mirror both in the vertical axis to obtain the other manifolds for the hyperbolic points.

For a discussion of lobe dynamics we follow the approach of Rom-Kedar *et al.* (1990). Consider a heteroclinic point $\mathbf{q} \in W^s_- \cap W^u_+$. Let $S[\mathbf{p}_-, \mathbf{q}]$ denote the segment of W^s_- from $\mathbf{p}_-$ to $\mathbf{q}$, and let $U[\mathbf{p}_+, \mathbf{q}]$ denote the segment of W^u_+ from $\mathbf{p}_+$ to $\mathbf{q}$. Then $\mathbf{q}$ is called a primary intersection point (PIP) if the segment of the stable manifold from $\mathbf{p}_-$ to $\mathbf{q}$ and the segment of the unstable manifold from $\mathbf{p}_+$ to $\mathbf{q}$ intersect only in $\mathbf{q}$, *i.e.* $S[\mathbf{p}_-, \mathbf{q}] \cap U[\mathbf{p}_+, \mathbf{q}] = \{\mathbf{q}\}$. Let $\mathbf{q}_1$ and $\mathbf{q}_2$ be two adjacent PIPs, *i.e.* there are no other PIPs on $S[\mathbf{q}_1, \mathbf{q}_2]$ and $U[\mathbf{q}_1, \mathbf{q}_2]$. The region enclosed by these segments of W^s_- and W^u_+ is called a lobe. See figure 2.4 for an example.

Points that are on a manifold must stay on that manifold for all iterations of the Poincaré map. This implies that a heteroclinic point $\mathbf{q}$ can only be mapped onto another heteroclinic point, because $\mathbf{q}$ must remain on both manifolds. Suppose that $\mathbf{q}_1$ is mapped onto $\mathbf{q}_2$, and $\mathbf{q}_2$ is mapped onto $\mathbf{q}_3$ after one iteration of the mapping. Choose a point $\mathbf{a} \in S[\mathbf{q}_1, \mathbf{q}_2]$ as shown in figure 2.4. This point then would be mapped onto a point $\mathbf{b} \in S[\mathbf{q}_2, \mathbf{q}_3]$. Going around the region enclosed by $S[\mathbf{q}_1, \mathbf{q}_2]$ and $U[\mathbf{q}_1, \mathbf{q}_2]$ in a clockwise way, one encounters $\mathbf{q}_1$, $\mathbf{q}_2$, and $\mathbf{a}$ in that order. Going around the mapped region, the order is $\mathbf{q}_2$, $\mathbf{b}$ and $\mathbf{q}_3$. This mapping cannot hold since it violates orientation preservation.

When $\mathbf{q}_1$ is mapped onto $\mathbf{q}_3$ and $\mathbf{q}_2$ is mapped onto $\mathbf{q}_4$, the orientation preservation holds. This implies that lobe L_1 is mapped onto L_3, and L_2 is mapped onto L_4, and so forth. In figure 2.4, the region bounded by (i) the segment of the unstable manifold (solid

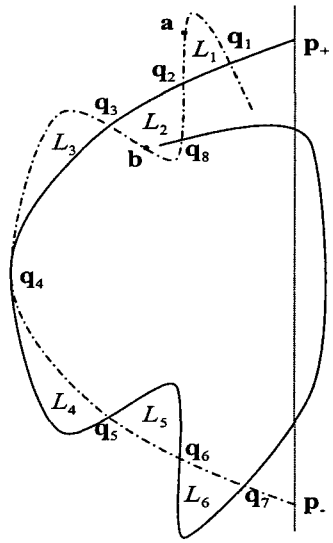

Figure 2.4: An example view of the manifolds. The solid line is the unstable manifold of $\mathbf{p}_+$*, the dash-dotted line is the stable manifold of* $\mathbf{p}_-$*.* $\mathbf{q}_1$ *through* $\mathbf{q}_7$ *are PIPs,* $\mathbf{q}_8$ *is not.* L_1 *through* L_6 *are lobes. Point* **a** *is on* $S[\mathbf{q}_1, \mathbf{q}_2]$*, point* **b** *is on* $S[\mathbf{q}_2, \mathbf{q}_3]$*.*

line) from $\mathbf{p}_+$ to $\mathbf{q}_4$, (ii) the segment of the stable manifold (dash-dotted line) from $\mathbf{p}_-$ to $\mathbf{q}_4$, and (iii) these segments mirrored in the vertical dotted line, will be called the vortex interior. As can be concluded from figure 2.4, a lobe initially in the vortex interior, like lobe L_2, is transported to the vortex exterior after one iteration, lobe L_4. Thus L_2 is a detrainment lobe. Lobe L_3 is initially in the vortex exterior, but is transported to the vortex interior, lobe L_5. L_3 is called an entrainment lobe. The entrainment and detrainment lobes combined are known as a turnstile. Mappings of the turnstile backward and forward in time are also called turnstiles. Note that in this geometry there are two entrainment and detrainment lobes due to the symmetry mentioned before.

The entrainment and detrainment of lobes provides a mechanism for transport of fluid. The amount of fluid entrained and detrained is equal to the lobe area. Due to area preservation of the Poincaré map, the area is the same for all lobes. The lobe area is computed in two different ways.

The first method is to obtain the stable and unstable manifolds by direct integration of the advection equations. The resulting data for the manifolds can then be used to calculate the area enclosed by the manifolds. This method is valid for all values of ϵ, the amplitude of perturbation.

For small values of ϵ, there is another method for determining the lobe area, which gives an order ϵ approximation of the area. This so-called Melnikov theory is discussed in section 2.1.5.

It is also possible to expand the motions of manifolds and lobes to three-dimensional flows. Beigie *et al.* (1994) showed how to apply these concepts to the three-dimensional case.

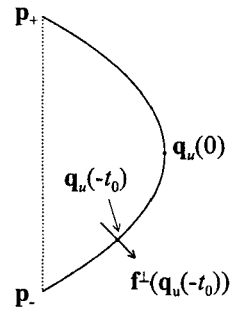

Figure 2.5: Definitions for the parametrisation of Ψ_e, and the moving coordinate system $\mathbf{f}^{\perp}(\mathbf{q}_u(-t_0))$.

2.1.5 Melnikov theory

Consider the expression for the unperturbed stream function, equation (2.2), and introduce the perturbation (2.5). For small values of the amplitude of perturbation ϵ the stream function can be expanded in a Taylor expansion in powers of ϵ. The advection equations resulting from the expansion are

$$\begin{aligned} \frac{dx}{dt} &= f_1(x,y) + \epsilon g_1(x,y,t) + O(\epsilon^2), \\ \frac{dy}{dt} &= f_2(x,y) + \epsilon g_2(x,y,t) + O(\epsilon^2). \end{aligned} \tag{2.10}$$

Melnikov (1963) developed an analytical technique that predicts the (signed) distance between W^u_- and W^s_+ along the unperturbed manifold for small ϵ. Using this technique it is possible to calculate this distance to the first order of ϵ without solving (2.10) explicitly. This first-order term is known as the Melnikov function.

To determine the Melnikov function for the observed geometry, the approach given by Wiggins (1992) is followed.

The first step in constructing the Melnikov function is to develop a parametrisation of the unperturbed manifolds $\Psi_{e,w}$, the separatrices. In the following discussion, we only consider Ψ_e. The result is also valid for Ψ_w by the symmetry with respect to the vortex position. Let $\mathbf{q}_u(t)$ denote a heteroclinic trajectory (*i.e.* a trajectory that includes both hyperbolic points) of the unperturbed velocity field that coincides with Ψ_e. Note that t is now a parameter. See also figure 2.5. The point $\mathbf{q}_u(0)$ denotes a unique point on Ψ_e. Then, by uniqueness of solutions, the point $\mathbf{q}_u(-t_0)$ denotes the unique point on Ψ_e that takes a time t_0 to flow to $\mathbf{q}_u(0)$. As t_0 varies from $-\infty$ to ∞, all points on Ψ_e are included. Thus $\mathbf{q}_u(-t_0)$ provides a valid parametrisation.

The next step is to define a moving coordinate system along the unperturbed manifold Ψ_e. The vector $\mathbf{f}^{\perp}(\mathbf{q}_u(-t_0)) = (-f_2(\mathbf{q}_u(-t_0)), f_1(\mathbf{q}_u(-t_0))$ is perpendicular to Ψ_e at each point $\mathbf{q}_u(-t_0)$ (figure 2.5). Thus $\mathbf{f}^{\perp}(\mathbf{q}_u(-t_0))$ is moved along Ψ_e by varying t_0, and the distance between the perturbed manifolds W^u_- and W^s_+ will be measured along $\mathbf{f}^{\perp}(\mathbf{q}_u(-t_0))$.

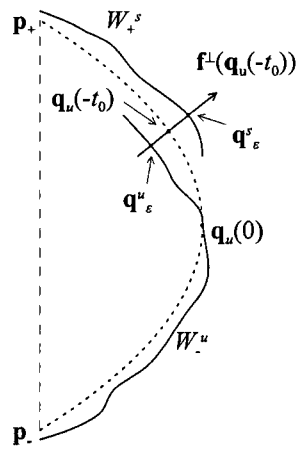

Figure 2.6: Geometry of the distance between W^u_- and W^s_+.

Under perturbation, for small amplitude of perturbation ϵ, W^u_- and W^s_+ intersect $\mathbf{f}^\perp(\mathbf{q}_u(-t_0))$ transversely in the points $\mathbf{q}^u_\epsilon$ and $\mathbf{q}^s_\epsilon$, see figure 2.6. Melnikov (1963) defined the following 'signed' distance measurement:

$$d(t_0,\epsilon) = \frac{\mathbf{f}^\perp(\mathbf{q}_u(-t_0)) \cdot (\mathbf{q}^u_\epsilon - \mathbf{q}^s_\epsilon)}{\|\mathbf{f}(\mathbf{q}_u(t_0))\|}, \tag{2.11}$$

where $\cdot$ denotes the usual vector dot product, and $\|...\|$ is the Euclidean length. This length is given by

$$\|\mathbf{f}(\mathbf{q}_u(-t_0))\| = \sqrt{(f_1(\mathbf{q}_u(-t_0)))^2 + (f_2(\mathbf{q}_u(-t_0)))^2}. \tag{2.12}$$

Next, Taylor-expand (2.11) with respect to ϵ:

$$d(t_0,\epsilon) = \epsilon \frac{\mathbf{f}^\perp(\mathbf{q}_u(-t_0)) \cdot \left(\frac{\partial \mathbf{q}^u_\epsilon}{\partial \epsilon}|_{\epsilon=0} - \frac{\partial \mathbf{q}^s_\epsilon}{\partial \epsilon}|_{\epsilon=0} \right)}{\|\mathbf{f}(\mathbf{q}_u(-t_0))\|} + O(\epsilon^2). \tag{2.13}$$

Melnikov (1963) showed that the numerator of the $O(\epsilon)$ term of (2.13) can be expressed as (see also Guckenheimer & Holmes (1983))

$$\begin{aligned} &\mathbf{f}^\perp(\mathbf{q}_u(-t_0)) \cdot \left(\frac{\partial \mathbf{q}^u_\epsilon}{\partial \epsilon}|_{\epsilon=0} - \frac{\partial \mathbf{q}^s_\epsilon}{\partial \epsilon}|_{\epsilon=0} \right) \\ &= \int_{-\infty}^{\infty} [\mathbf{f}(\mathbf{q}_u(t)) \cdot \mathbf{g}(\mathbf{q}_u(t), t+t_0)]\, dt \\ &= \int_{-\infty}^{\infty} [f_1(\mathbf{q}_u(t)) g_2(\mathbf{q}_u(t), t+t_0) - f_2(\mathbf{q}_u(t)) g_1(\mathbf{q}_u(t), t+t_0)]\, dt. \end{aligned} \tag{2.14}$$

This expression is commonly known as the Melnikov function and is denoted by $M(t_0)$. Thus the distance between W^u_- and W^s_+ is given by

$$d(t_0,\epsilon) = \epsilon \frac{M(t_0)}{\|\mathbf{f}(\mathbf{q}_u(-t_0))\|} + O(\epsilon^2). \tag{2.15}$$

Melnikov (1963) also showed that simple zeros of $M(t_0)$ (*i.e.* $M(t_0) = 0, \partial M/\partial t_0 \neq 0$) imply simple zeros of $d(t_0, \epsilon)$, for ϵ sufficiently small. Zeros of $M(t_0)$ thus correspond to intersection points of stable and unstable manifolds in the Poincaré map. Also note that $\|\mathbf{f}(\mathbf{q}_u(-t_0)\| \to 0$ exponentially fast as $t_0 \to \pm\infty$ which implies that $|d(t_0, \epsilon)| \to \infty$ as $t_0 \to \pm\infty$. This is a reflection of the unbounded oscillation of W^u_- and W^s_+ near $\mathbf{p}_+$ and $\mathbf{p}_-$, respectively.

The next step is to calculate the area of a lobe. This area can also be calculated from the Melnikov function. The area μ is given by

$$\mu = \epsilon \int_{t_{0,1}}^{t_{0,2}} |M(t_0)| dt_0 + O(\epsilon^2), \tag{2.16}$$

where $t_{0,1}$ and $t_{0,2}$ are the values of t_0 corresponding to the PIPs defining the lobe. For a detailed derivation of this formula, see Rom-Kedar *et al.* (1990).

Thus the integral of the Melnikov function between two adjacent PIPs gives an $O(\epsilon)$ approximation to the area of the lobe defined by the PIPs. Equation (2.16) is only valid for lobes defined by PIPs that are outside of sufficiently small neighbourhoods of $\mathbf{p}_+$ and $\mathbf{p}_-$, again due to the unbounded oscillation of one of the manifolds near those points. Since all lobes have the same area one is free to choose a lobe that is not near $\mathbf{p}_+$ and $\mathbf{p}_-$.

2.2 Rotating fluids

2.2.1 Taylor-Proudman theorem

The presence of background rotation has a profound effect on fluid motion. In a co-rotating reference frame the flow can be described by (see *e.g.* Pedlosky 1979)

$$\frac{\partial \mathbf{v}}{\partial t} + (\mathbf{v} \cdot \nabla)\mathbf{v} + 2\boldsymbol{\Omega} \times \mathbf{v} = -\frac{1}{\rho}\nabla p + \frac{1}{2}\nabla(\Omega^2 r^2) - \nabla\Phi_{gr} + \nu\nabla^2\mathbf{v}, \tag{2.17}$$

where $\mathbf{v}$ is the velocity vector relative to the rotating reference frame, $\boldsymbol{\Omega}$ the background rotation, ρ the density, p the pressure, r the radius measured from the rotation axis, Φ_{gr} the gravitational potential, and ν the kinematic viscosity. It is customary to rewrite equation (2.17) using the reduced pressure P, defined as $P = p - \frac{1}{2}\rho\Omega^2 r^2 + \rho\Phi_{gr}$:

$$\frac{\partial \mathbf{v}}{\partial t} + (\mathbf{v} \cdot \nabla)\mathbf{v} + 2\boldsymbol{\Omega} \times \mathbf{v} = -\frac{1}{\rho}\nabla P + \nu\nabla^2\mathbf{v}. \tag{2.18}$$

It is useful to write (2.18) as a dimensionless equation to determine the relative importance of each term or to compare flows of different scales. This can be done by introducing the following dimensionless variables

$$\tilde{\mathbf{v}} = \frac{\mathbf{v}}{U}, \quad \tilde{P} = \frac{P}{\rho\Omega U L}, \quad \tilde{t} = \Omega t, \quad \tilde{\mathbf{x}} = \frac{\mathbf{x}}{L},$$

in which U is a typical velocity scale and L a typical length scale. Here it is tacitly assumed that characteristic horizontal and vertical length scales are of the same order. Using these variables, equation (2.18) takes the following form

$$\frac{\partial \tilde{\mathbf{v}}}{\partial \tilde{t}} + Ro(\tilde{\mathbf{v}} \cdot \tilde{\nabla})\tilde{\mathbf{v}} + 2\mathbf{k} \times \tilde{\mathbf{v}} = -\tilde{\nabla}\tilde{P} + E\tilde{\nabla}^2\tilde{\mathbf{v}}, \tag{2.19}$$

with $\mathbf{k} = \boldsymbol{\Omega}/|\boldsymbol{\Omega}|$ the unit vector in axial direction, $Ro = U/\Omega L$ the Rossby number, and $E = \nu/\Omega L^2$ the Ekman number. The Rossby and Ekman numbers represent the importance of inertial and viscous forces relative to the Coriolis force, respectively.

If the flow is quasi-stationary with $Ro \ll 1$ and $E \ll 1$, then equation (2.19) can be simplified considerably. In this case the motion is governed by

$$2\mathbf{k} \times \mathbf{v} = -\nabla P, \tag{2.20}$$

omitting the tildes for convenience. The flow is now governed by a balance of the Coriolis force and the pressure gradient force. Both forces act perpendicular to the local velocity. An important dynamical property of these so-called geostrophically balanced flows is obtained by taking the curl of equation (2.20) with the assumption that the flow is incompressible. This result is known as the Taylor-Proudman theorem:

$$\frac{\partial \mathbf{v}}{\partial z} = 0. \tag{2.21}$$

The Taylor-Proudman theorem expresses that a geostrophically balanced flow is independent of the axial coordinate, *i.e.* it is a two-dimensional flow.

2.2.2 Spin-up

In the laboratory experiments the shear flow is generated by a change in rotation velocity. Consider a rotating tank filled with water that is in a solid-body rotation. A change in the rotation speed from Ω to $\Omega + \Delta\Omega$ causes the water to adapt to the new rotation speed, to again end up in solid-body rotation eventually. The characteristic timescale for the adaptation process is the so-called Ekman timescale T_E:

$$T_E = \frac{H}{(\nu\Omega)^{1/2}}. \tag{2.22}$$

Because of the change in rotation speed there is a change in vorticity ω in the co-rotating frame of reference. The absolute vorticity ω_a is the vorticity relative to the laboratory frame of reference, and is thus defined as $\omega_a = \omega + 2\Omega$. In two-dimensional, inviscid, barotropic, incompressible flows the absolute vorticity is a conserved quantity. So ω_a does not change in the initial stage of the adaptation process. Then ω_a is given by

$$\omega_a = (2\Omega + 2\Delta\Omega) - 2\Delta\Omega. \tag{2.23}$$

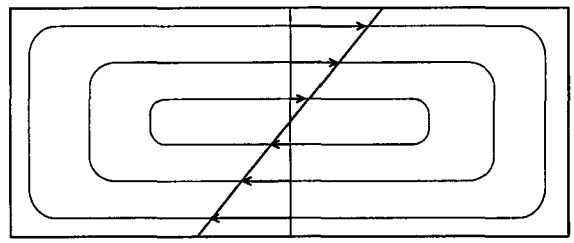

Figure 2.7: Schematic top view of the initial flow after spin-up. In the centre of the tank to good approximation a linear velocity profile $u = \alpha y$ is present.

Thus it follows with the definition of the absolute vorticity that the vorticity relative to the co-rotating frame of reference is

$$\omega = -2\Delta\Omega. \tag{2.24}$$

The relative vorticity appears as the source term for the Poisson equation $\nabla^2\Psi = -\omega$, which can be used to calculate the stream function Ψ in the co-rotating reference frame

$$\nabla^2\Psi = 2\Delta\Omega. \tag{2.25}$$

For $\Delta\Omega$ a single step, equation (2.25) was solved in a rectangular domain by van Heijst *et al.* (1990). The solution consists of a single cell of concentric closed streamlines, spanning the domain. This solution is schematically depicted in figure 2.7. For a domain of much greater length than width, there is to good approximation a linear shear flow $u = \alpha y$ at the centre of the domain. The value of the shear strength α is found using $\omega = (\nabla \times \mathbf{v})_z = -\alpha$

$$\alpha = 2\Delta\Omega. \tag{2.26}$$

So an increase in rotation speed causes an anticyclonic motion in the tank, and vice versa.

In this work a constant shear with a small perturbation is generated. This is achieved by a stepwise increase in rotation speed, followed by a small harmonic oscillation of the rotation speed. The applied rotation speed is given by

$$\Omega(t) = \Omega_0 + \Delta\Omega[1 + \epsilon\cos(\omega_s t)]\Theta(t), \tag{2.27}$$

with Ω_0 the initial rotation speed, $\Delta\Omega$ the stepwise increase of the rotation speed, and $\Theta(t)$ the unit step function. The evolution of the shear α in time follows from equation (2.26)

$$\alpha(t) = 2\Delta\Omega[1 + \epsilon\cos(\omega_s t)]\Theta(t). \tag{2.28}$$

Note that these approximations are not valid near the walls of the tank. Viscous effects near the walls cause the formation of a boundary layer to match with zero velocity at the wall. It is also only valid for times small compared to the Ekman timescale. Effectively this results in a window of time of about 1-2 minutes in which the approximations hold.

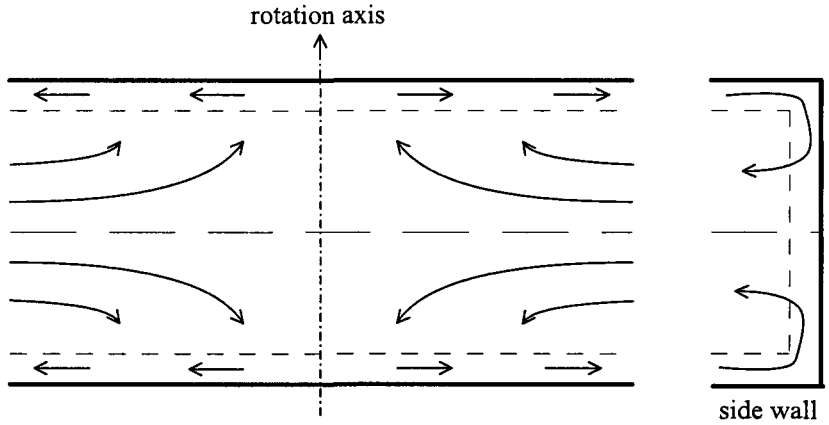

Figure 2.8: Secondary circulation driven by the Ekman layers during spin-up. The boundary layers are confined by the lines with short dashes. The line with the long dashes indicates the plane of symmetry.

2.2.3 Ekman boundary layers

The change of rotation velocity mentioned in section 2.2.2 has another important consequence. This change causes a secondary circulation, which is largely responsible for the decay of vortices as well as the background shear flow.

Consider a fluid between two parallel disks, rotating about a common vertical axis. Initially, both disks rotate at angular velocity Ω. The fluid between the disks is in solid-body rotation. Then, at $t = 0$, the angular velocity of both disks is increased by a factor $(1 + \epsilon)$, with $0 < \epsilon \ll 1$. This is to insure that the Rossby number Ro remains small. Immediately after $t = 0$, Ekman layers will be formed at both disks. The reader is referred to Pedlosky (1979) or Kundu (1990) for more information on the formation process of Ekman layers. The formation is essentially established by diffusion of vorticity, so an associated formation time can be estimated:

$$\frac{\partial}{\partial t} \sim \nu \frac{\partial^2}{\partial z^2} \sim \frac{\nu}{\delta_E^2} \quad \rightarrow \quad T \sim \frac{\delta_E^2}{\nu} = \frac{(HE^{1/2})^2}{\nu} = \Omega^{-1}, \tag{2.29}$$

with $\delta_E = HE^{1/2} = (\nu/\Omega)^{1/2}$ the Ekman layer thickness. Since the disks rotate faster than the fluid in the interior of the flow region, the Ekman layers will produce a radial outflow. This outflow is compensated by an axial flow towards each disk. This secondary circulation is known as Ekman suction. See figure 2.8 for an illustration of the circulation.

The Ekman suction brings interior fluid closer to the axis of rotation, and increases thereby its azimuthal velocity in order to conserve angular momentum. In the Ekman layers an outward flow is generated by acceleration due to viscous forces. Note that this circulation is present in infinite and finite domains; on a finite domain the circulation is closed by flow through a boundary layer at the side wall. In case of the top disk being absent, the fluid surface coincides with the plane of symmetry in figure 2.8. Here

the influence of the water-air interface is neglected, since it accounts for a much smaller boundary layer and thus far less circulation.

The Ekman mechanism causes horizontal velocities in the fluid interior to decay exponentially until a new solid-body rotation is achieved. The characteristic timescale is again the Ekman timescale T_E (equation (2.22)). Ekman decay is far more efficient than viscous decay. Viscous decay has an associated timescale T_ν

$$\frac{\partial}{\partial t} \sim \nu \frac{\partial^2}{\partial z^2} \sim \frac{\nu}{H^2} \quad \rightarrow \quad T_\nu = \frac{H^2}{\nu}. \tag{2.30}$$

Inserting realistic values in equations (2.22) and (2.30) shows that the viscous timescale is a factor 100 larger than the Ekman timescale. Therefore viscous decay is neglected henceforth.

Chapter 3

Numerical simulations

In this chapter the methods and results of numerical simulations using two different techniques are presented. The two techniques used are contour kinematics and advection of passive markers.

Three parameters determine the flow field associated with a point vortex in a harmonically time-perturbed linear shear: (i) the distance from the vortex position to the stagnation points $r_s = \sqrt{\gamma/2\pi\alpha_0}$, (ii) the perturbation frequency ω_s, and (iii) the perturbation amplitude ϵ. Distances can be made dimensionless by using the characteristic distance r_s as the scaling factor. Times can conveniently be multiplied by $f_s = \omega_s/2\pi$ in order to make them dimensionless.

Throughout this report the parameters for the numerical simulations are in meter-kilogram-second (MKS) units.

3.1 Contour kinematics

Numerical simulations using the contour kinematics method have been performed to construct the manifolds. The contour kinematics method is used to monitor in time a contour, defined by passive markers connected by small linear segments. If enough markers are used, the line appears smooth. Initially the markers form a circle.

Integrating the advection equations (2.1) for each marker results in the evolution of the contour in time. The contour will get stretched and folded by the flow. When at a time $t = t^*$ the distance between two markers becomes larger than a preset value, or when the angle between neighbouring linear segments is less than 120° an extra marker is added to retain a smooth line. This marker is placed on the initial circle, and then the calculations up to $t = t^*$ are repeated for this marker. When the distance between two neighbouring markers becomes very small a marker is removed to save computational time. All time integrations are performed using a variable-order Runge-Kutta scheme. For a thorough description of the contour kinematics method, see Meleshko & van Heijst (1994).

The area μ of a surface S enclosed by any deformed curve C was calculated using

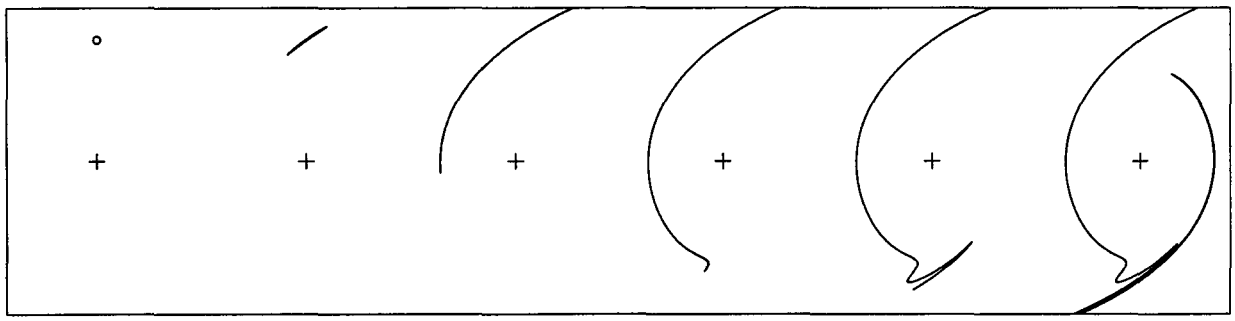

Figure 3.1: Evolution in time of a contour initially located around $\mathbf{p}_+$. *The contour is shown from* $t = 0$ *(leftmost picture), to* $t = 5T$ *(rightmost picture). There is a time step* T *between each picture. The cross depicts the vortex location. The flow parameters are* $\gamma = 20\pi$, $\alpha_0 = 1$, $\omega_s = 1.6\pi$, $\epsilon = 0.1$. *At* $t = 0$ *the contour is defined by 10 markers. The number of markers increases to 200 at* $t = T$, *871 at* $t = 2T$, *2218 at* $t = 3T$, *4502 at* $t = 4T$, *and finally 8218 at* $t = 5T$.

Stokes' theorem

$$\mu = \iint_S dx\, dy = \frac{1}{2} \oint_C (-ydx + xdy) \approx \frac{1}{2} \sum_{i=1}^{M} (x_i y_{i+1} - y_i x_{i+1}), \tag{3.1}$$

with a summation over the M markers of contour C.

3.1.1 Manifolds and lobe area

The following method is used to construct the manifolds. A small contour is placed around a hyperbolic fixed point at $t = 0$. Due to the hyperbolic nature of this point the contour in time will be compressed exponentially in one direction and elongated exponentially in another direction. Soon after the simulation has started the contour resembles a line. The contour is monitored in time, as depicted in figure 3.1. It will get stretched right along the unstable manifold of the hyperbolic point. Thus the unstable manifold is constructed. Because of symmetry, the stable manifold can be obtained by mirroring the unstable manifold in the y-axis. The unstable and stable manifolds of the other hyperbolic point result from mirroring both manifolds in the point where the vortex is located, halfway between $\mathbf{p}_+$ and $\mathbf{p}_-$. Two example results are shown in figure 3.2, for amplitude of perturbation $\epsilon = 0.1$ and $\epsilon = 0.5$. This is only part of the real heteroclinic tangle. Since there are infinitely many intersection points of the stable and unstable manifolds there is also an infinite number of lobes. These lobes get more and more elongated and intertwined when approaching $\mathbf{p}_\pm$, and are as such not suitable for visualisation.

The next task is to find the coordinates of the intersection points of the stable and unstable manifolds. To obtain these coordinates, the subsequent points in the contours are connected with straight line segments. The cross of these line segments is considered the intersection point. Now it is possible to define a closed contour around a lobe. It

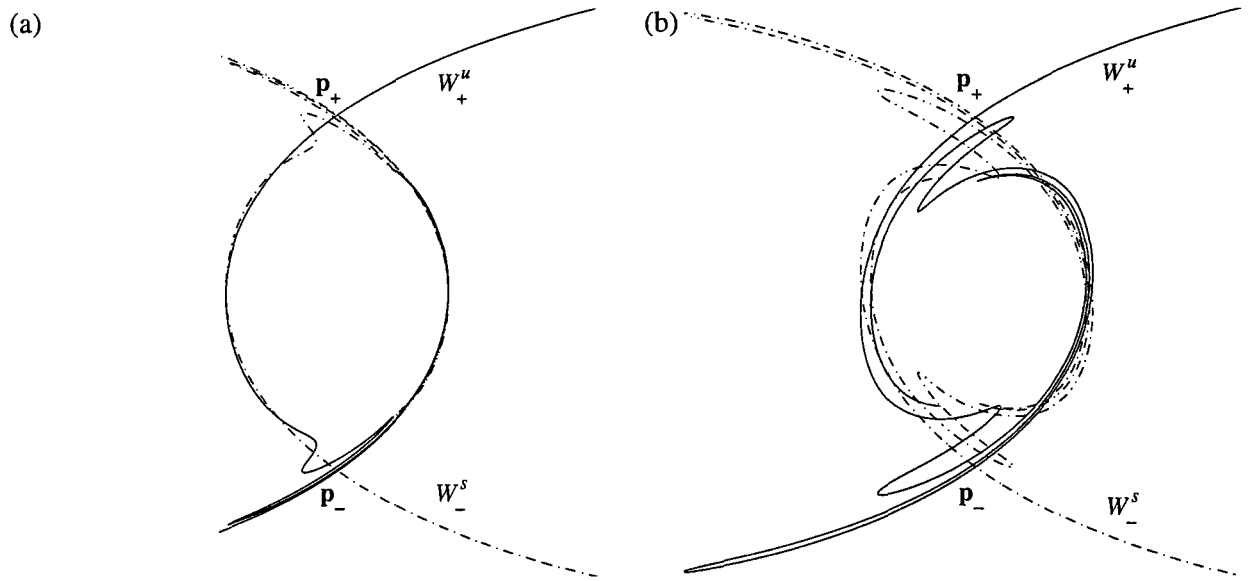

Figure 3.2: The heteroclinic tangle of a point vortex in a perturbed linear shear. The unstable manifold W^u_+ of $\mathbf{p}_+$ and the stable manifold W^s_- of $\mathbf{p}_-$ are shown. The other two manifolds are omitted for clarity. The flow parameters are $\gamma = 20\pi$, $\alpha_0 = 1$, $\omega_s = 1.6\pi$. For (a) the amplitude of perturbation $\epsilon = 0.1$, for (b) $\epsilon = 0.5$.

consists of segments of the manifolds between two intersection points, complemented with the coordinates of the intersection points. Applying equation (3.1) to this contour gives the lobe area μ.

For small perturbation amplitudes ϵ the Melnikov method is also a valid technique for calculating the lobe area μ. A parametric expression for the unperturbed manifold is needed to derive the Melnikov function $M(t_0)$. This parametrisation is derived in appendix A. The Melnikov function itself is derived in appendix B. The result is

$$M(t_0) = \frac{\gamma}{2\pi} P\left(\frac{\omega_s}{2\alpha_0}\right) \sin(\omega_s t_0), \tag{3.2}$$

where the function $P(p)$ was evaluated numerically; it is depicted in figure 3.3.

The lobe area μ according to Melnikov theory is found using equation (2.16)

$$\mu = \frac{\epsilon\gamma}{\pi\omega_s} P\left(\frac{\omega_s}{2\alpha_0}\right). \tag{3.3}$$

The lobe area is proportional to the amplitude of perturbation ϵ. To compare the results for the lobe area from the numerical simulations with the results from Melnikov theory, they are both depicted in figure 3.4, scaled by ϵ. Since the term in equation (3.3) outside of the function P has an inverse proportionality to ω_s, the graph is shown with the inverse of this parameter on the x-axis. There is a remarkably good agreement between the prediction from Melnikov theory and the results from direct numerical integration. Clearly,

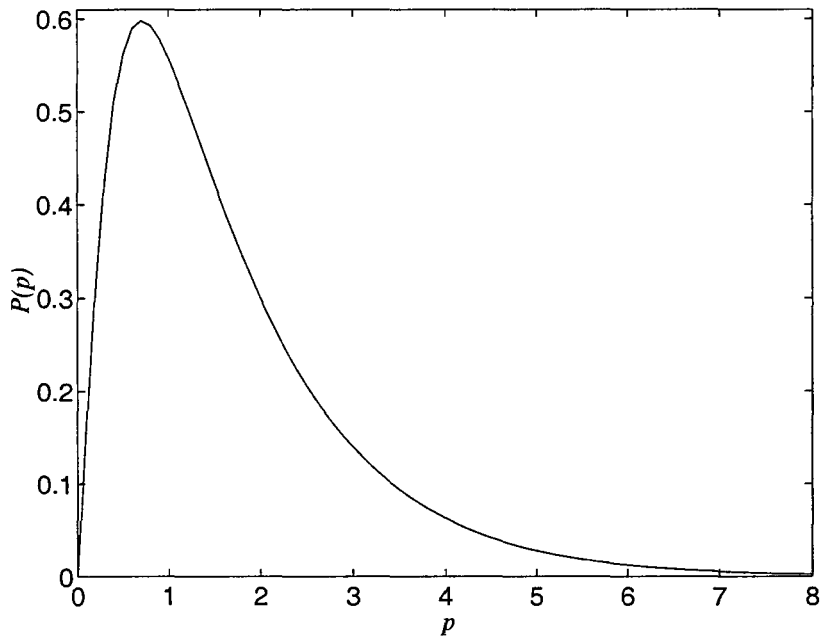

Figure 3.3: The function $P(p)$ from the Melnikov function $M(t_0)$ in equation (3.2).

the Melnikov function provides a very good approximation of the lobe area for values of ϵ at least up to 0.2. Near $1/\omega_s = 0$ the lobe area rapidly approaches zero. For large perturbation frequencies there is little fluid exchange per cycle between the vortex interior and exterior.

The full dependence of the lobe area on shear strength α_0 and perturbation frequency ω_s is more complicated. This dependence is depicted in figure 3.5. For this graph $\gamma = 1$ is chosen. Since the lobe area μ is directly proportional to γ this is a convenient choice. On the axes $\mu/\epsilon = 0$, and μ/ϵ is still very small near the axes. This behaviour is evident from the graph of the function P, as shown in figure 3.3. In the limit of $\alpha_0 \to 0$ or $1/\omega_s \to 0$ the function P rapidly approaches zero. For $1/\omega_s \to 0$ this trend is further aided by the $1/\omega_s$ term outside of the function P.

The shape of figure 3.4 can be obtained from figure 3.5. In figure 3.5, monitor μ/ϵ while travelling over a horizontal line at $\alpha_0 = 1$ and multiply by 20π to account for the vortex strength γ.

3.1.2 Stretching and folding

Transport between the vortex core and the exterior can be understood by studying the intersection between the stable and unstable manifolds of the hyperbolic points $\mathbf{p}_\pm$ in the Poincaré map. This intersection gives rise to another important dynamical effect, chaotic fluid particle motion.

Chaotic fluid particle motion may result when regions of fluid in the flow are strongly stretched and folded. In the flow under study the heteroclinic tangle provides the folding

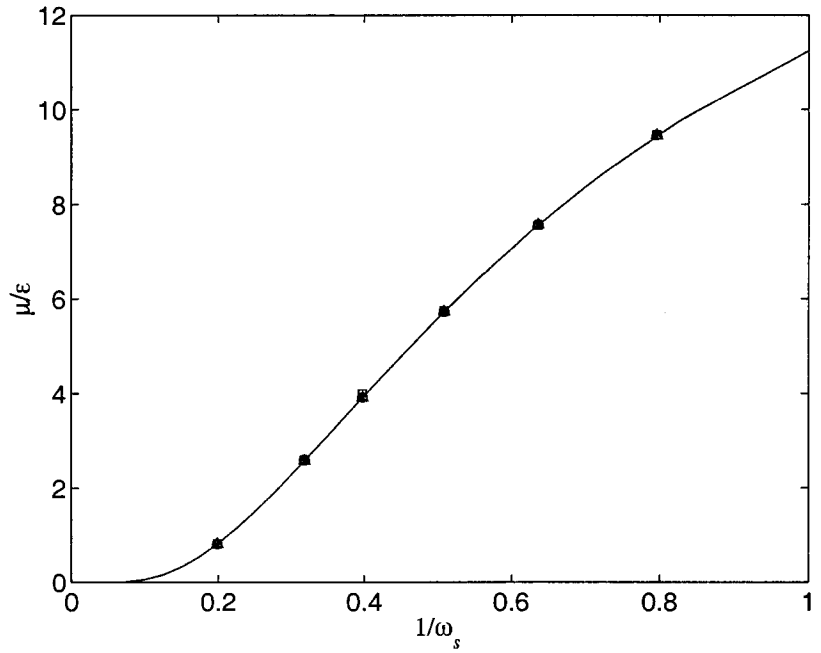

Figure 3.4: Lobe area μ, divided by ϵ, as function of $1/\omega_s$. The solid line represents the value calculated with the Melnikov function, while the individual data points are direct results from the numerical simulations for different values of ϵ: $\square$ $\epsilon = 0.01$, $\triangle$ $\epsilon = 0.05$, $\circ$ $\epsilon = 0.1$, $*$ $\epsilon = 0.2$. The other parameters are $\gamma = 20\pi$ and $\alpha_0 = 1$.

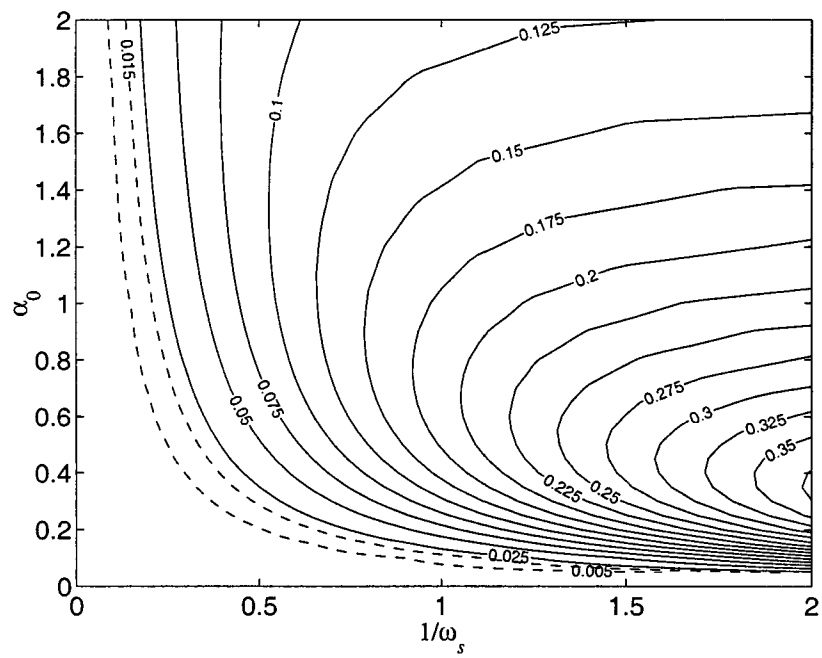

Figure 3.5: Lobe area μ, divided by ϵ, as function of $1/\omega_s$ and α_0. For this graph $\gamma = 1$. On the axes $\mu/\epsilon = 0$.

mechanism, while the fixed points $\mathbf{p}_\pm$ provide the stretching mechanism. To visualise these mechanisms four contours were placed at different locations in the heteroclinic tangle. The resulting evolution is shown in figure 3.6. The advection of the contours in the heteroclinic tangle is shown for five subsequent times $t = 0, T, ..., 4T$. Initially the contours have a circular shape. They are stretched and contracted by the influence of the fixed points, and folded along the unstable manifolds. The initial position of the contours relative to the stable manifold determines the eventual direction in which they are transported. The two contours at the interior side of the stable manifold (the dash-dotted and solid thick lines) remain in the vortex interior, at least for the observed time. The other two contours (the dashed and dotted thick lines) are transported away from the vortex interior from $t = 2T$ and on.

The deformation due to the unstable manifold is also apparent. The solid and dash-dotted contours are folded along the unstable manifold near $\mathbf{p}_-$, and subsequently stretched on the way up. Then (for $t = 4T$) the onset of the next folding along the unstable manifold is visible. This mechanism of stretching and folding is known as the Smale horseshoe map, and is further illustrated by Rom-Kedar *et al.* (1990) and Wiggins (1992) for a related perturbed flow. There are chaotic fluid particle trajectories in the sense of Smale horseshoes (Wiggins 1998).

The mechanisms of stretching and folding have a profound effect on the contour length. This effect has been investigated by monitoring the contour length stretch of a contour, initially around the fixed point $\mathbf{p}_+$, in time, for different values of perturbation frequency $f_s = \omega_s/2\pi$. First define the length stretch λ as

$$\lambda(t) = \frac{l(t)}{l(0)}, \tag{3.4}$$

where $l(t)$ is the contour length at time t, and $l(0)$ is thus the initial length at $t = 0$. The results are shown in figure 3.7.

At first, the stretch evolves the same for all cases. This is due to the exponential stretch near $\mathbf{p}_+$, as is shown in appendix C. The slope of the length stretch graph for $t < 2.5$ is about the same for all cases shown. A calculation of the slope on this region for the unperturbed case gives a result of 0.60, while from the crude analysis in appendix C a slope of $\log[\exp(\sqrt{2})] \approx 0.61$ is expected. So it is plausible that the initial stretch is due to the vicinity of the hyperbolic fixed point $\mathbf{p}_+$.

Next is the increase in contour length after the initial stretch near the hyperbolic fixed point, from $t = 2.5$ and on. The dashed line indicates the stretch for the case of no perturbation. There is linear expansion, as is expected from a fully integrable velocity field. In the presence of perturbation, however, fluid particles may separate at an exponential rate. On a logarithmic scale an exponential increase results in a linear graph. All of the solid lines are approximately linear. However, there is an oscillation present on these lines. This oscillation is caused by the perturbation. The period of this oscillation is exactly the same as the period of the perturbation. The amplitude of the oscillation is smaller for the higher perturbation frequencies since then the sign of the perturbation changes rapidly. The perturbation changing sign causes the contour to fold. The higher the perturbation

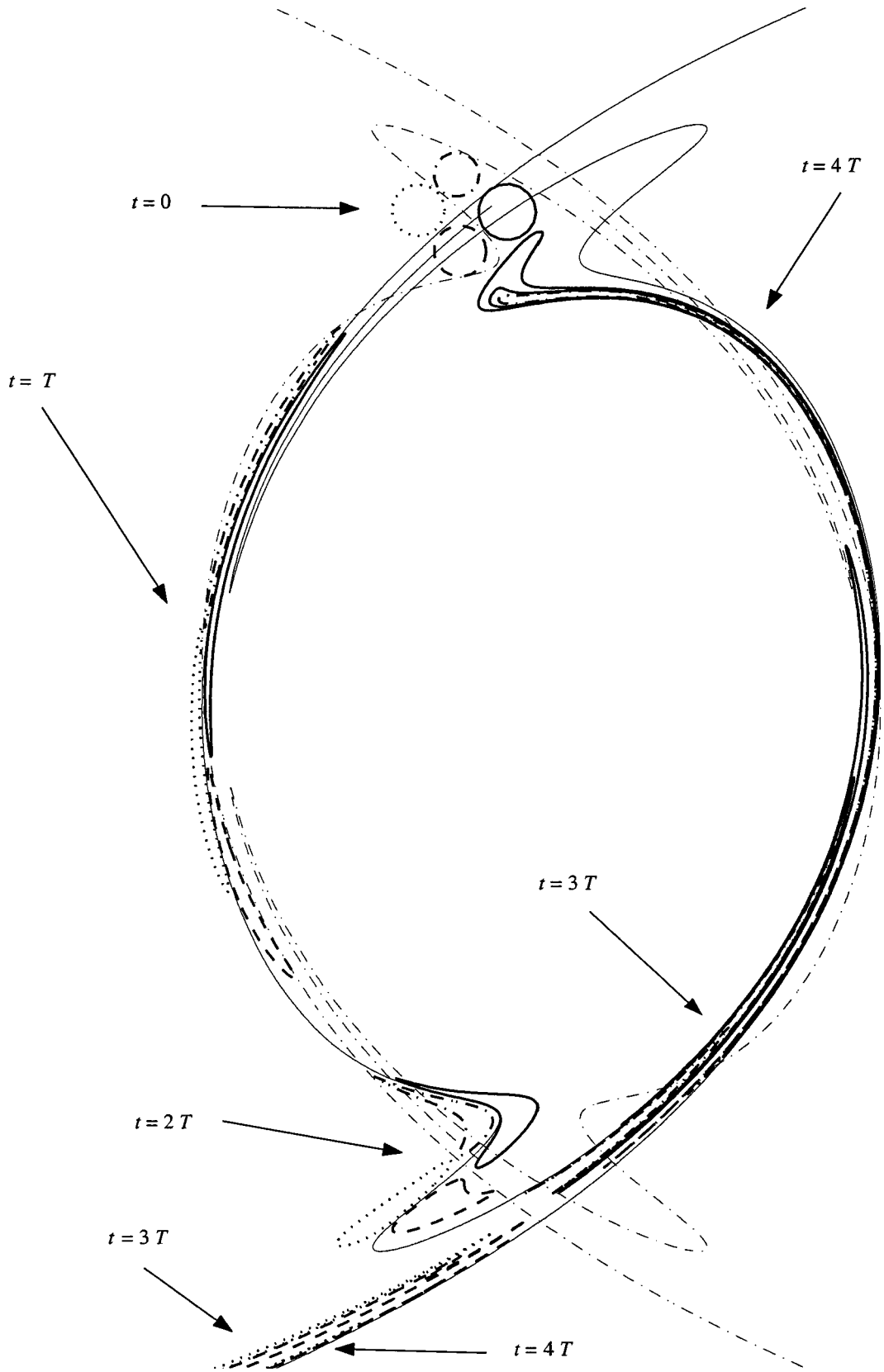

Figure 3.6: Advection of contours in the heteroclinic tangle. The stable manifolds are depicted by the thin dash-dotted lines, while the unstable manifolds are shown as thin solid lines. The contours are deformed by stretching and folding mechanisms in the flow.

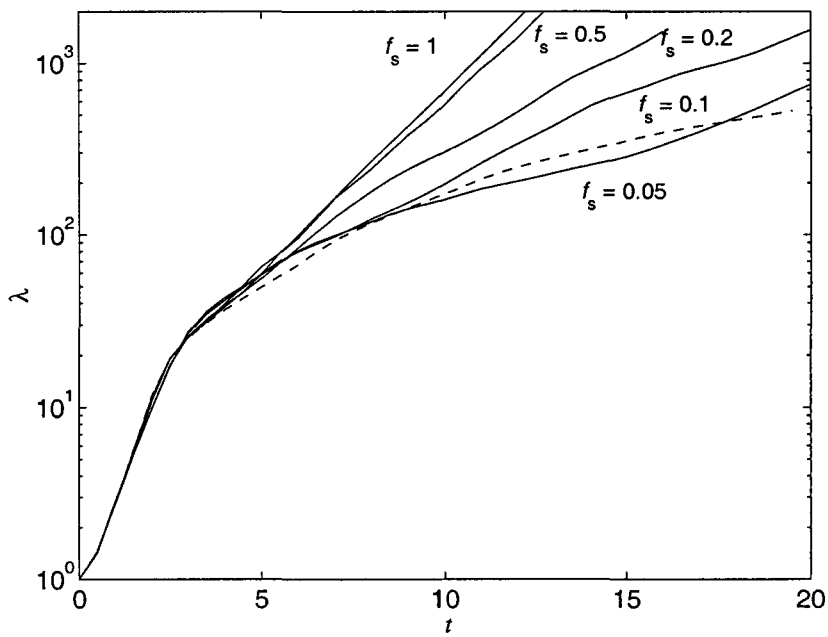

Figure 3.7: Length stretch λ of a contour, initially around the fixed point $\mathbf{p}_+$. The dashed line gives the length stretch for zero perturbation amplitude. The solid lines are for simulations with perturbation, with corresponding values of f_s. The other parameters are $\gamma = 8\pi$, $\alpha_0 = 1$ and $\epsilon = 0.1$.

frequency, the more folds take place. More folds causes the length stretch to increase faster. Therefore the line of length stretch at the highest frequency is the steepest.

3.1.3 Vortex decay

As was mentioned in section 2.2.3, there is a secondary vertical circulation known as Ekman suction in rotating fluids. The Ekman suction causes vortices to decay exponentially. As was confirmed experimentally by Kloosterziel & van Heijst (1992), the associated characteristic e-folding time is the Ekman timescale T_E. The same exponential decay can be observed in the (unperturbed) shear flow, with the same timescale. However, the vortex circulation in experiments also decays by stripping of vorticity. The stripping is assumed to cause an exponential decay of the vortex circulation. To determine the influence of vortex decay, the vortex strength γ is made time dependent according to

$$\gamma(t) = \gamma_0 \exp\left(-\frac{t}{T}\right), \tag{3.5}$$

with γ_0 the initial vortex strength and T the timescale of the exponential decay. Realistic laboratory values were used for the other flow parameters. The results for contour kinematics simulations with decaying vortex strength are depicted in figure 3.8, a picture of the evolution at $t = 70$. The decaying vortex causes the vortex region to decrease in area. This is evident from the lines approaching the centre. The contour does not circle around the vortex as far. In the case of $T = 100$, it does not even reach the other side of the vortex. There is however no great difference between the dashed line (no decay) and the dash-dotted line. So as long as the vortex decay timescale is not too small, the expected behaviour in experiments is not fundamentally different from the (non-decaying) simulations.

3.1.4 Perturbation of vortex strength

Another interesting case is the flow due to a perturbed point vortex in a constant linear shear. In this case the shear strength α is constant in time, while the vortex strength γ is dependent on time as

$$\gamma(t) = \gamma_0[1 + \epsilon\cos(\omega_s t)], \tag{3.6}$$

in which γ_0 is the basic-state vortex strength, while ϵ and ω_s are again amplitude and frequency of perturbation, respectively.

The resulting flow has been studied in the same way as in section 3.1.1. An example result is shown in figure 3.9. This figure closely resembles figure 3.2a. The difference between the two figures is the relative orientation of the stable and unstable manifold. The perturbation in the vortex reaching its maximum corresponds in the previous configuration to the perturbation of the shear reaching its minimum. There is a half-period phase shift between these two configurations. This is also evident from the Melnikov function changing sign, as is derived in appendix B. The Melnikov function essentially gives a signed distance between the stable and unstable manifolds (equation (2.15)), therefore the change of sign.

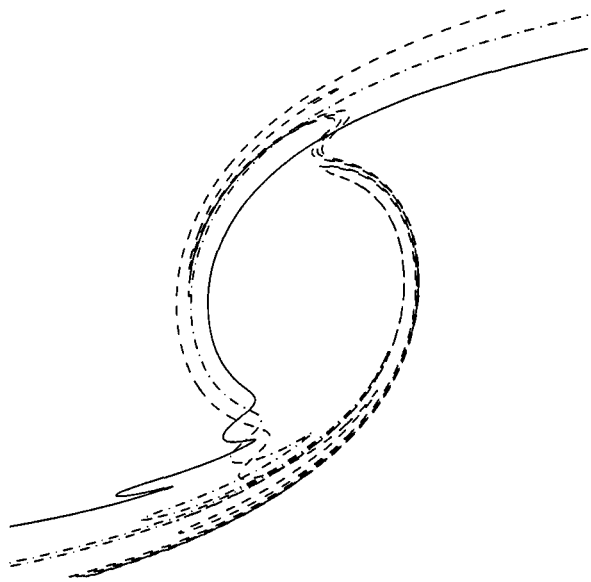

Figure 3.8: Shape at $t = 70$ of a contour initially around the hyperbolic point $\mathbf{p}_+$. The vortex strength γ decayed exponentially. The dashed line shows the shape in absence of vortex decay. The dash-dotted line shows the shape for a decaying timescale $T = 239$, a realistic laboratory value for Ekman decay. The solid line is the shape for a decaying timescale $T = 100$. The other flow parameters were $\alpha_0 = 0.1$, $\epsilon = 0.4$, $\omega_s = 0.2\pi$, $\gamma_0 = 0.0064$.

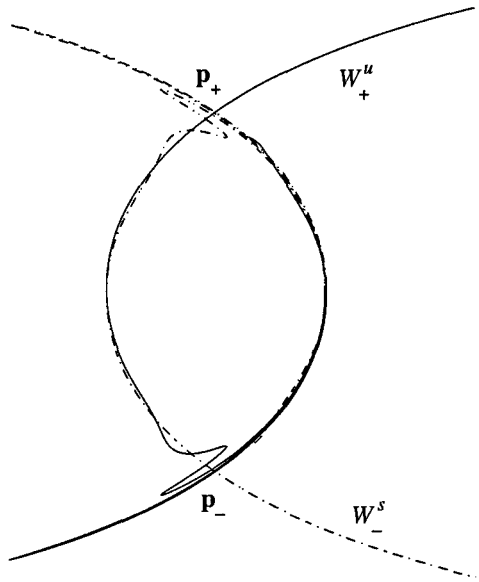

Figure 3.9: Heteroclinic tangle of the flow due to a perturbed point vortex in a linear shear. Again, only the unstable manifold W^u_+ of $\mathbf{p}_+$ and the stable manifold W^s_- of $\mathbf{p}_-$ are shown. The other two manifolds are omitted for clarity. The flow parameters are $\gamma_0 = 20\pi$, $\alpha = 1$, $\omega_s = 1.6\pi$, and $\epsilon = 0.1$.

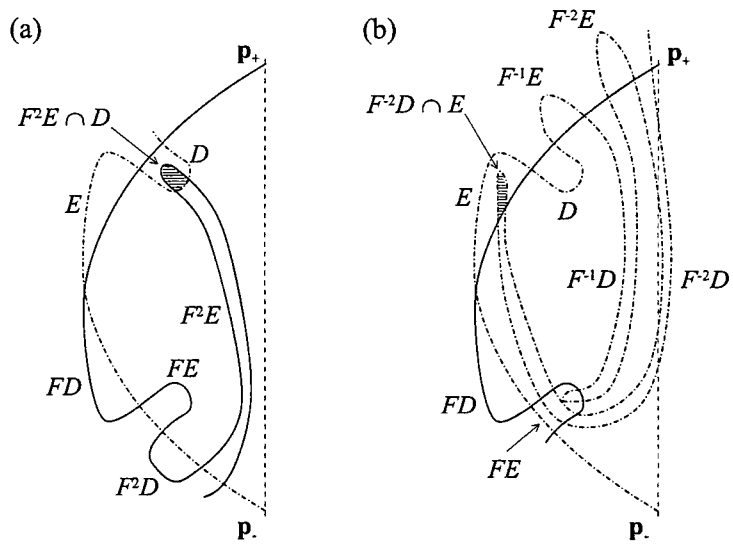

Figure 3.10: Example view of the heteroclinic tangle, to illustrate the intersection of lobes: (a) $e_3 = \mu(F^2E \cap D)$, (b) $e_3 = \mu(E \cap F^{-2}D)$.

3.2 Particle transport

In this section another method to investigate fluid transport is presented. This method consists of advecting a large amount of passive particles (order 10^3) in time as prescribed by the advection equations (2.1). The advection equations are integrated using a fourth-order Runge-Kutta scheme with constant time step.

3.2.1 Escape time and area

The time for a particle to stay in the vortex interior depends on the particle's initial conditions. Rom-Kedar *et al.* (1990) define this time as the residence time. A volume of fluid therefore has an associated residence time distribution. The residence time varies for particles inside the volume. The notion of a residence time distribution is an important concept in mixing systems. For example, the amount of product from a reaction in a catalytic reactor will be primarily dependent on the time spent in the reactor. Heat and mass transfer are similarly influenced by the residence time distributions. In the present case, the residence time distribution provides information on the origin of fluid being mixed, and the direction and distribution of fluid transport.

Consider the heteroclinic tangle in figure 3.10. The entrainment lobe (section 2.1.4) is labelled as E, and D is the detrainment lobe. In one cycle of the perturbation, E is entrained into and D is detrained from the vortex interior (see section 2.1.4). E and D have equal area due to incompressibility of the flow. This area has already been denoted by μ. Some mappings F^kE and F^lD are also shown.

The question to be answered is: How long does it take fluid to escape from the vortex interior given that it started there? Rom-Kedar *et al.* (1990) argue that this question

is equivalent to: How long does it take fluid to escape the vortex interior given that is initially in the entrainment lobe E? To answer this question, consider fluid that is in lobe E initially. It is clear that this fluid enters the vortex interior in the next cycle. After some more cycles, say $k-1$ cycles, part of the original fluid may be found in a detrainment lobe D. This part of fluid is given by the intersection of lobe E after $k-1$ cycles with lobe D, $F^{k-1}E \cap D$. This portion of fluid will then escape the vortex interior during the next cycle. Define e_k to be that portion of fluid, *i.e.* the volume of fluid in lobe E at cycle 0 that escapes on the kth cycle:

$$e_k = \mu(F^{k-1}E \cap D), \quad k = 1, 2, ... \tag{3.7}$$

For $k \leqslant 0$ it is clear that $e_k = 0$. The escape time distribution is now given by $e_k/\mu(E)$. Note that, by incompressibility, (3.7) can alternatively be written as

$$e_k = \mu(E \cap F^{-k+1}D), \quad k = 1, 2, ... \tag{3.8}$$

This is illustrated in figure 3.10.

A related quantity is the escape area a_k. This factor gives the volume of fluid in the vortex interior on cycle 0 that escapes on cycle k. Effectively a_k gives the area of fluid entrained in cycle 0 that is still present in the vortex interior at cycle k. Thus as $a_k \to 0$ all of the fluid entrained in cycle 0 has been transported out of the vortex interior. Fluid leaving the interior on the kth cycle must be in D at cycle $k-1$, and thus in $F^{-k+1}D$ at cycle 0. However, not all of this fluid was in the interior at cycle 0. There may be other 'earlier' intersections of $F^{-k+1}D$ and $F^{-l}E$, $0 \leqslant l \leqslant k$, and these should not be counted. So it follows that

$$a_k = \mu(F^{-k+1}D) - \sum_{l=0}^{k} \mu(F^{-k+1}D \cap F^{-l}E). \tag{3.9}$$

This equation can be simplified. By incompressibility $\mu(F^{-k+1}D) = \mu(D) = \mu(E)$. From (3.8) it follows that

$$e_{k-l} = \mu(F^{-k+1}D \cap F^{-l}E). \tag{3.10}$$

With these simplifications, equation (3.9) can be written as

$$a_k = \mu(E) - \sum_{l=0}^{k} e_{k-l} = \mu(E) - \sum_{l=1}^{k} e_l. \tag{3.11}$$

Thus, to compute a_k, only the factors e_k must be known (with the lobe area $\mu(E)$).

In order to calculate the escape time and escape area distribution the entrainment lobe E closest to $\mathbf{p}_+$ was filled with tracer particles on a regular grid. Five calculations were performed, each with the following settings: $\gamma = 20\pi$, $\alpha = 1$, $\epsilon = 0.2$. The perturbation frequencies ω_s used are 0.4π, 0.8π, 1.6π, 2π and 3.2π. The lobe area decreases with increasing perturbation frequency (see figure 3.5). In the first case the lobe was filled

with $N = 1631$ particles on a grid with mesh 0.01. In the second case $N = 7808$ with again a mesh 0.01. For the third case $N = 4741$ with a mesh 0.02. In the fourth case $N = 3202$ with a mesh 0.005. For the fifth case $N = 2752$ with mesh 0.002. The number of particles $e(k)$ that escapes in cycle k is a measure for e_k. $e(k)/N$ is used as approximation of e_k/μ. A similar argument applies to $a(k)/N$ as approximation of a_k/μ. The approximations get more reliable with decreasing mesh. Results for $e(k)/N$ and $a(k)/N$ are presented in figures 3.11 and 3.12. For all five cases 50 cycles were elapsed.

In the observed geometry there are two detrainment lobes. One detrainment lobe can be found near $\mathbf{p}_+$, accounting for fluid transport from the vortex interior along the unstable manifold of $\mathbf{p}_-$ away from the vortex. On the opposite side there is another detrainment lobe, transporting fluid from the vortex interior along the unstable manifold of $\mathbf{p}_+$ away from the vortex. Therefore the escape times and escape areas can be divided in escape to the $+x$-direction ('right') and escape to the $-x$-direction ('left'). Therefore, in figures 3.11 and 3.12 the diamonds in the graphs of $e(k)/N$ depict the transport to the left, and the circles denote transport to the right. The total transport per cycle is shown by the squares. In the graphs of $a(k)/N$, the fraction between the plusses and the dots has escaped to the right while the fraction above the dots has escaped to the left.

From figure 3.11 it can be concluded that fluid from the entrainment lobe is detrained earlier for lower perturbation frequencies ω_s. This is evident as the graphs of $a(k)/N$ approach zero. For $\omega_s = 1.6\pi$ the graph of $a(k)/N$ (plusses) goes below 0.1 in the 47th cycle, at $t \approx 59$. For $\omega_s = 0.8\pi$ this happens during the 6th cycle, at $t \approx 15$. In the last case, $\omega_s = 0.4\pi$, $a(k)/N$ goes below 0.1 halfway through the 3rd cycle, at $t \approx 13$. In figure 3.11a,b ($\omega_s = 0.4\pi$) there even is evidence of an immediate (cycle 0) overlap of entrainment and detrainment lobes, resulting in a $\sim \frac{3}{4}$ detrainment during the first cycle: $e(1)/N \approx 0.75$.

There is an asymmetrical distribution of the transport to the left and to the right. Fluid entrained from the top left is in larger part transported towards the top right. In the extreme case ($\omega_s = 0.4\pi$) more than 80% of this fluid is transported to the top right. This paradoxical behaviour is due to the lobe dynamics. For entrained fluid to be transported from the top left to the bottom left it first has to circle around the vortex to reach the correct detrainment lobe, while the other detrainment lobe (responsible for transport to the right) is encountered first.

In order to determine the asymptotic behaviour of $a(k)/N$ for large k, two further plots are shown in figure 3.13. Figure 3.13a contains a log-linear plot of $a(k)/N$, while figure 3.13b contains a log-log plot. In case of exponential behaviour for large k the graph appears as a straight line in the log-linear plot. For power-law behaviour the graph is a straight line in the log-log plot. Exponential behaviour indicates a probability of escape that is constant for all k, while power-law behaviour implies a probability of escape that decreases with increasing k (Rom-Kedar *et al.* 1990). The graph for $\omega_s = 0.4\pi$ is omitted. This graph rapidly approaches zero, and due to the finite resolution (finite number of particles) causes large stepwise changes on a logarithmic scale. Many more particles need to be used in order to determine the asymptotic behaviour for this frequency. These steps, albeit smaller, are also visible in the graph for $\omega_s = 0.8\pi$ ($\times$).

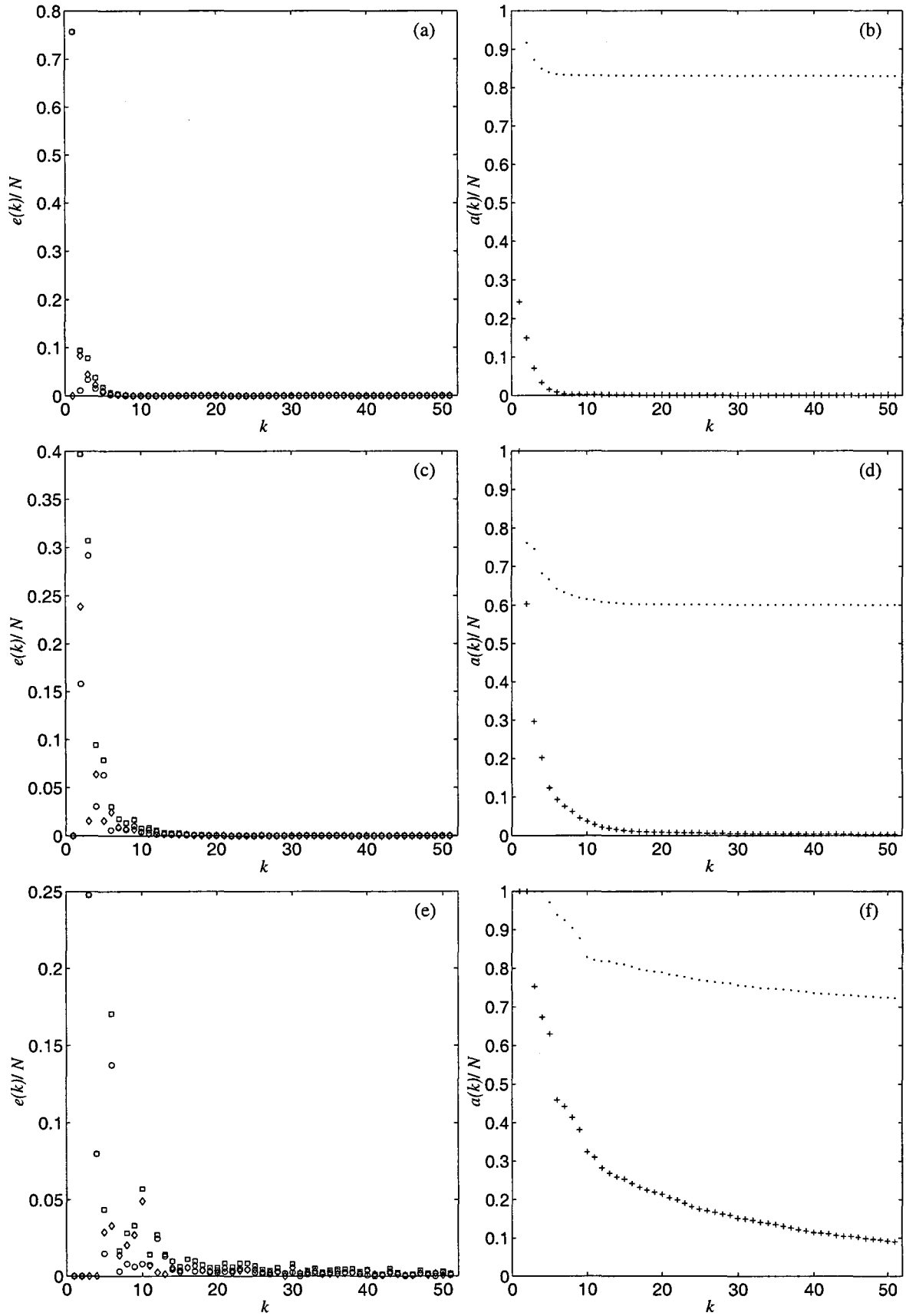

Figure 3.11: Normalised escape times $e(k)/N$ and normalised escape areas $a(k)/N$ for three different perturbation frequencies ω_s: (a,b) 0.4π, (c,d) 0.8π, (e,f) 1.6π. For symbols see text.

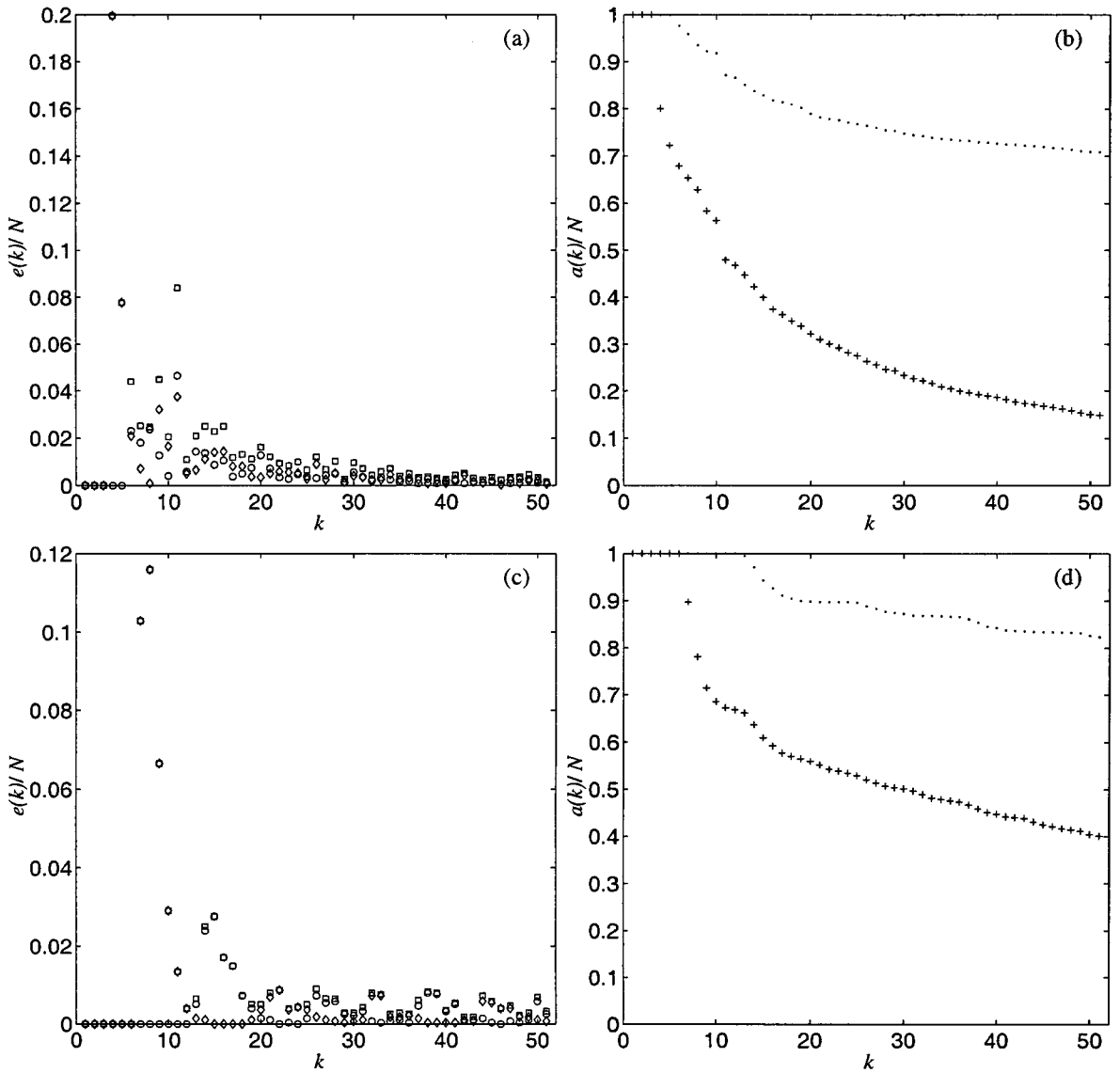

Figure 3.12: Normalised escape times $e(k)/N$ and normalised escape areas $a(k)/N$ for two different perturbation frequencies ω_s: (a,b) 2π, (c,d) 3.2π. For symbols see text.

From figure 3.13a an exponential behaviour is apparent for $\omega_s = 3.2\pi$ ($\circ$). For $\omega_s = 1.6\pi$ ($+$) there is also probable exponential behaviour. Figure 3.13b indicates possible power-law dependence for $\omega_s = 2\pi$ ($*$). Both graphs give no clear indication of the behaviour for $\omega_s = 0.8\pi$ ($\times$).

The area of fluid initially in the entrainment lobe that escapes the vortex interior during the kth cycle is given by $e_k = \mu(E \cap F^{-k+1}D)$. There are two ways to obtain the geometry of the intersection $E \cap F^{-k+1}D$. The first method is to compute the boundaries of the lobes E and $F^{-k+1}D$ and find the area of their intersection. The other method is to track area elements (or tracer particles) of the interior of lobe E to determine the area (or number

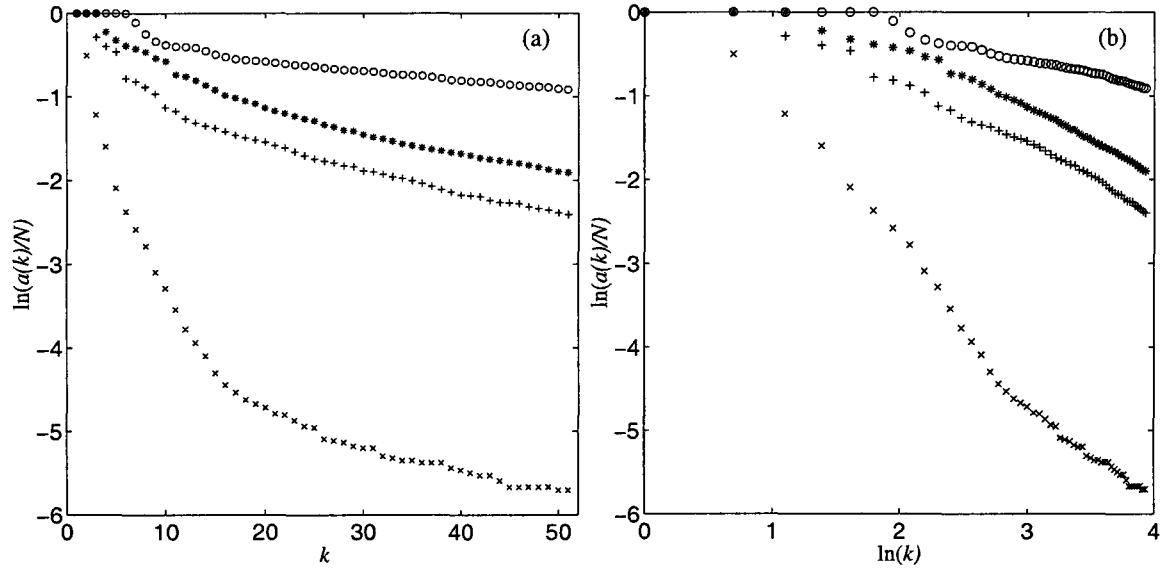

Figure 3.13: Normalised escape areas $a(k)/N$: (a) log-linear plot, (b) log-log plot. Perturbation frequencies ω_s: 0.8π ($\times$), 1.6π ($+$), 2π ($*$), 3.2π ($\circ$).

of particles) that escapes at each cycle. Although the first method is theoretically more satisfying, it also presents a substantial difficulty. Due to exponential stretch the lobe boundary is elongated considerably. For contour kinematics this means that each time step takes a longer computation time. After only a few periods this method is practically unusable. Therefore the second method is used. The parameters are the same as for the calculations of the escape times and escape areas.

An example result, for $\omega_s = 0.8\pi$, is shown in figure 3.14. Two other results, for $\omega_s = 0.4\pi, 1.6\pi$, are shown in appendix D. The other two cases were omitted, since the entrainment lobes are very narrow here and thus not suitable for visualisation. For large k, it appears as if the structures are composed of a number of isolated area elements. However, this is a result of using a finite number of non-deforming area elements. This also causes the fluctuations in the $e(k)/N$ graph for large k. When using a larger number of tracers these fluctuations will be smaller. Thus here is another manifestation of the complicated nature of the heteroclinic tangle. It also demonstrates the difficulties one would encounter when using a scheme that tracks the lobe boundaries, with the lobe interior becoming increasingly narrow.

3.2.2 Poincaré section

The obtained data can also be used to make a Poincaré section. All the actual positions of the particles after each cycle are drawn in a single plot. They are all also mirrored in the origin to account for the other entrainment lobe. For the case of $\omega_s = 1.6\pi$ the result is presented in figure 3.15. The other four Poincaré sections are given in appendix E. Three clearly distinct regions are visible where no particle has penetrated. The largest region is

the vortex core, where no particles can penetrate due to the elliptic nature of the vortex centre. To the left and to the right of the vortex core there are two additional regions. These regions are absent or much smaller in the other Poincaré sections in appendix E. In order to study these regions in more detail, another simulation has been performed. One passive tracer was placed inside the left region. Then the Poincaré map was recorded for 500 cycles. The obtained Poincaré map is depicted in figure 3.16. The tracer alternates between the two regions left and right from the vortex core. If the tracer is situated in the left region on a time nT, it will be in the right region one period T later, and vice versa.

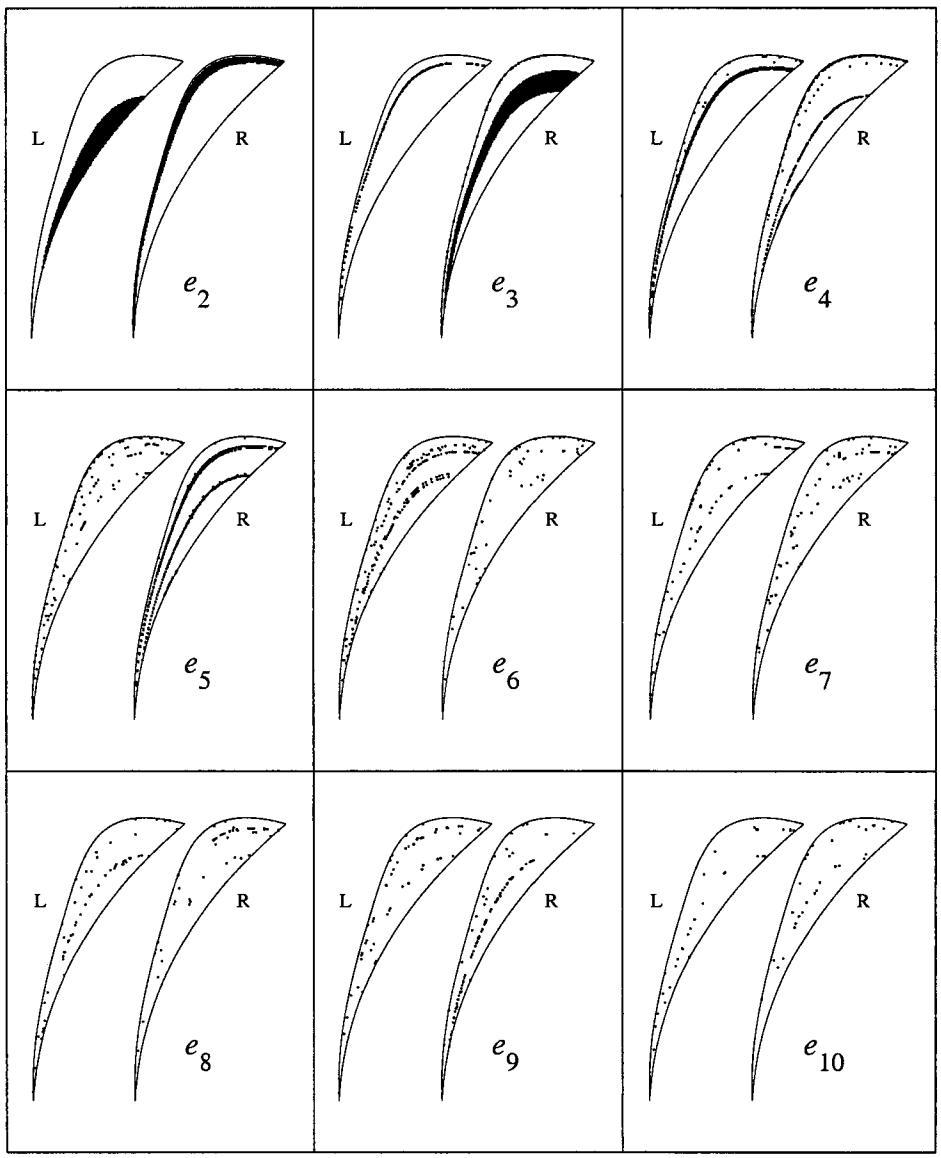

Figure 3.14: Geometry of $E \cap F^{-k+1}D$ for several values of k. 'L' stands for the intersection of E with the detrainment lobe transporting fluid to the left, 'R' is the intersection of E with the detrainment lobe transporting fluid to the right. Perturbation frequency $\omega_s = 0.8\pi$.

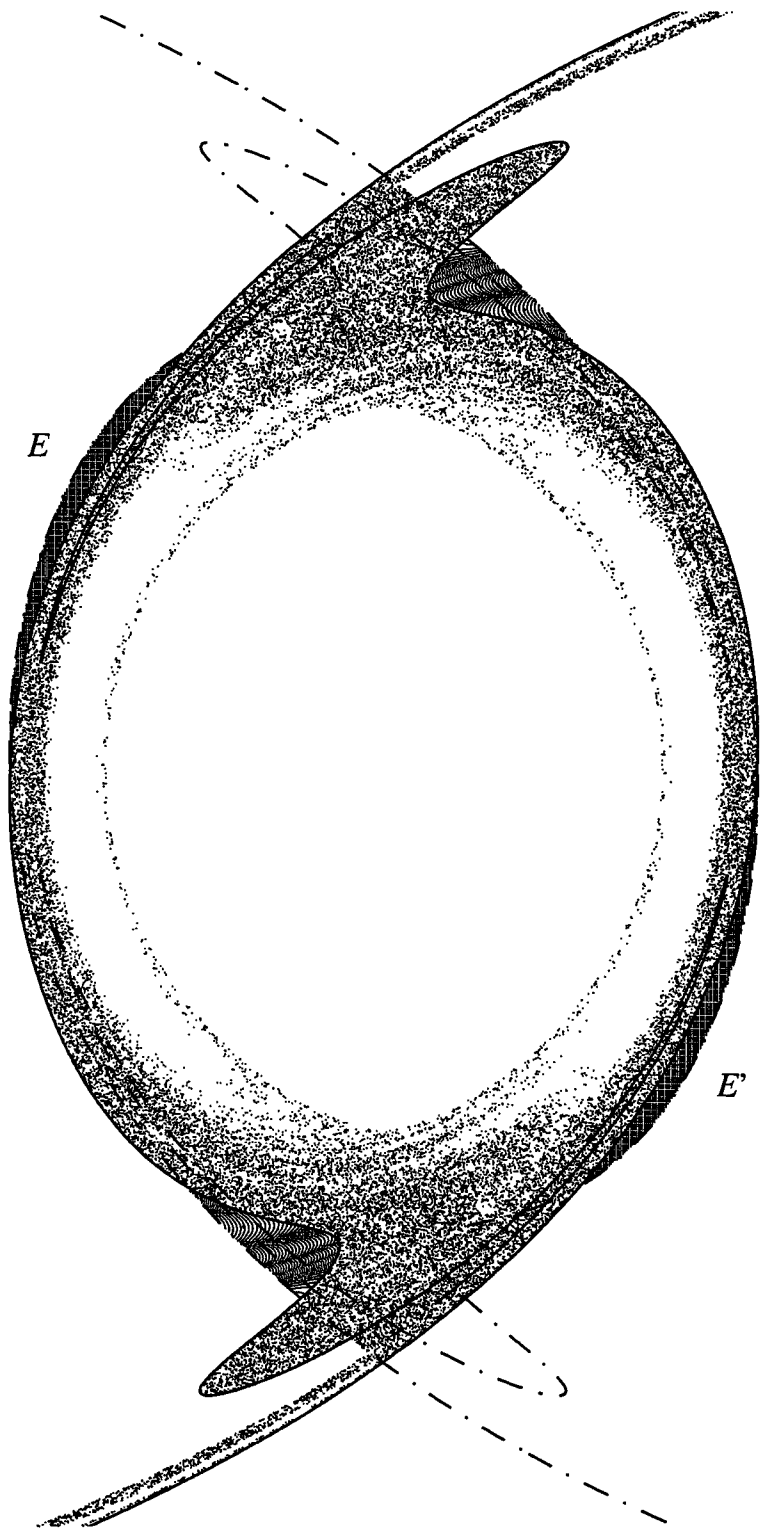

Figure 3.15: Poincaré section after 50 cycles of 2×1631 *particles initially in the entrainment lobes on a grid of mesh 0.01. The unstable manifolds are depicted with solid lines. The stable manifolds are shown with dash-dotted lines. Perturbation frequency* $\omega_s = 1.6\pi$.

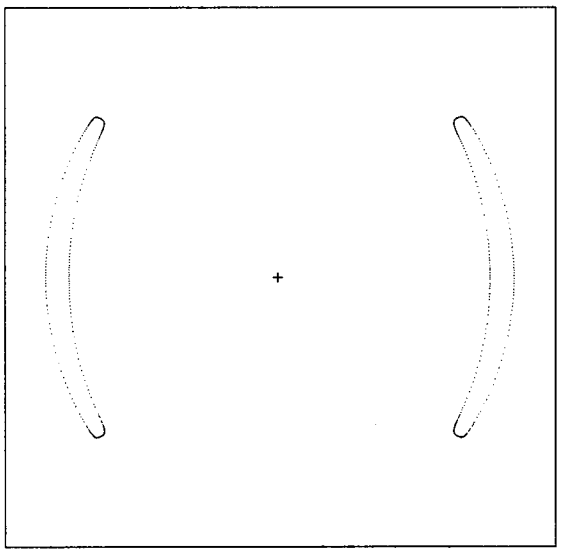

Figure 3.16: Poincaré map after 500 cycles of one tracer, initially placed in the region to the left of the vortex core (see figure 3.15). The cross indicates the vortex position.

The resulting structure is known as a resonance band or stochastic layer (see Arnol'd & Avez (1968) for more details). It has two associated coefficients p and q, originally defined for the unperturbed case. Consider an unperturbed closed invariant orbit with a periodic point. A tracer put there returns to its original position after p cycles of the Poincaré map. In the process it makes q complete revolutions around the vortex core. Define m as the number of cycles the tracer takes to complete one revolution, *i.e.* $m = p/q$. In the perturbed case these invariant orbits are destroyed. A resonance band remains. However, it is still possible to determine p and q, in the same vein as before. In this case there is a $p : q = 2 : 1$ resonance band.

In the Poincaré sections of the particle transport simulations at higher perturbation frequencies ($\omega_s = 2\pi, 3.2\pi$, see appendix E) higher-order resonance bands are visible, with $p : q = 4 : 1$ and $p : q = 10 : 1$. This behaviour is verified by additional simulations of the transport of one particle, placed in one of the blank subregions. For the duration of the 500 elapsed cycles the particle moves in a counterclockwise sense from one subregion to the next in one cycle. As the frequency increases more blank subregions will occur. Due to point symmetry in the vortex position only even values of p are allowed. It is plausible that frequencies between 2π and 3.2π can be found that give resonance bands with $p = 6, 8$.

Consider Rom-Kedar & Wiggins (1991) for another example of resonance bands in two-dimensional flows.

A further characteristic of the mixing efficiency is the area of the interior region that is involved in mixing, the so-called mixing area (Rom-Kedar *et al.* 1990). This can be considered a possible quantification of the mixing efficiency. The mixing area is apparent from the Poincaré sections as all the areas reached by particles, *i.e.* regions with black

dots. The mixing area gets better defined as more cycles have elapsed, and by using more particles as initial condition. Considering the five Poincaré sections it can be concluded that the mixing region is largest for the simulation with $\omega_s = 1.6\pi$. Both for larger and smaller frequencies the mixing area is smaller. So a maximum in mixing area is expected for a frequency close to $\omega_s = 1.6\pi$. Note, however, that the residence time of particles inside the interior region increases with increasing perturbation frequency. The residence time is an important property in reactive systems, as an indication of the time that the reactive components are in contact.

Chapter 4

Laboratory experiments

4.1 Experimental set-up

The laboratory experiments were performed in a rectangular plexiglass tank of dimensions length × width × height = 200×40×30 cm. This tank was mounted on a turntable, centred on the axis of rotation. It was filled with water to a depth of $H = 20$ cm. A perforated tube with 32 holes, distributed uniformly over a length of 15 cm, was placed vertically along the axis of rotation. A camera was mounted around 1 m above the water surface. Before each experiment, this system was allowed to spin up for at least half an hour at an angular velocity of $\Omega = 0.7$ rad s^{-1}, so that the water was in a solid-body rotation. Then a vortex was created by syphoning water through the perforated tube. The inward flow towards the tube is deflected by the Coriolis force, resulting in a cyclonic vortex. After a certain time the tube was removed manually. Next the shear was generated by a change in rotation velocity (see section 2.2.2). Two methods were used to study the flow. By adding dye the flow was visualised. Quantitative information was gained from particle tracking experiments. The experiments are discussed in sections 4.2 and 4.3, respectively.

4.1.1 Vortex characteristics

The vortex is created by syphoning fluid through the perforated tube. Due to the Coriolis force the inward flow towards the tube results in an increase of the circulation Γ. Consider, in two dimensions, a material contour C enclosing the sink tube. For a barotropic and inviscid fluid, the change in the circulation around this contour can be written as

$$\frac{D\Gamma}{Dt} = -2 \oint_C (\mathbf{\Omega} \times \mathbf{v}) \cdot d\mathbf{s}, \tag{4.1}$$

with $d\mathbf{s}$ an infinitesimal segment of contour C. The contour C is chosen to be a circle of radius r. It is assumed that the velocity $\mathbf{v}$ is of equal magnitude over this circle and that $\mathbf{v}$ points radially inward. Now the change in circulation is:

$$\frac{D\Gamma}{Dt} = -2\Omega v \cdot 2\pi r = -2\Omega q_{2D}, \tag{4.2}$$

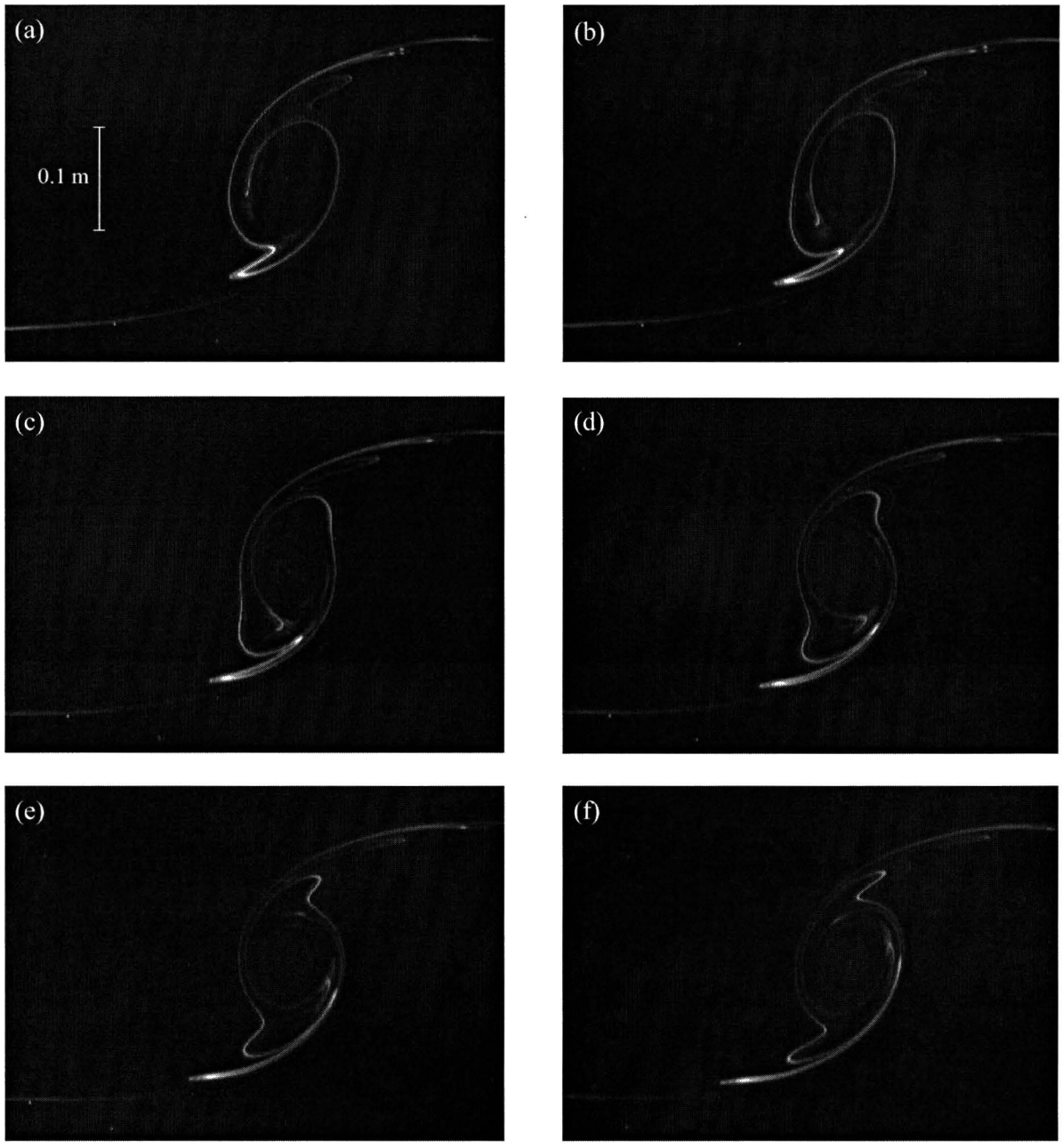

Figure 4.1: Time evolution of a dye experiment. The images are shown at time intervals of 2 s. The flow parameters are $\Delta\Omega = 0.05$ *rad* s^{-1}, $\Gamma = 6.3 \times 10^{-3}$ m^2 s^{-1}, $\epsilon = 0.4$, *and* $f_s = 0.1$ s^{-1}. *Between (a) and (f) one full period of the perturbation has elapsed.*

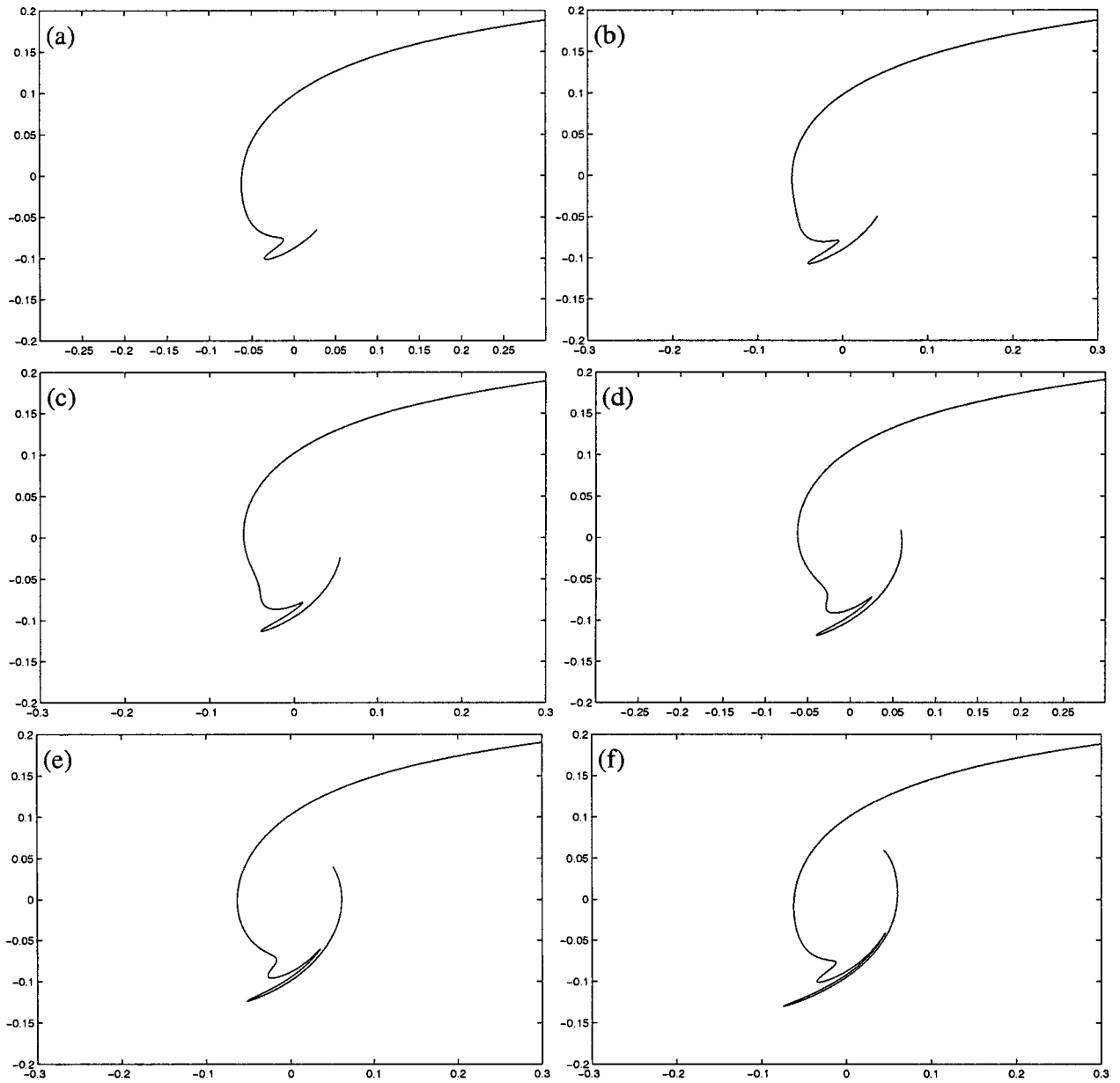

Figure 4.2: Time evolution of a numerical contour kinematics simulation. The images are shown at time intervals of 2 s. The flow parameters are $\gamma_0 = 6.3 \times 10^{-3}$, $\alpha_0 = 0.1$, $f_s = 0.1$, *and* $\epsilon = 0.4$. *Between (a) and (f) one full period of the perturbation has elapsed. Each image (a)–(f) corresponds in phase of the perturbation to the same image (a)–(f) in figure 4.1.*

with q_{2D} a two-dimensional area flux. To account for the depth of the fluid H, q_{2D} is equivalent to q_{3D}/H in three dimensions. Since the three-dimensional flow rate q_{3D} is negative (fluid is being extracted), the change in circulation is positive. For a fluid volume V removed in this way at a constant flow rate q_{3D}, the resultant circulation is

$$\Gamma = \frac{2\Omega V}{H}. \tag{4.3}$$

The circulation is not constant in time. As was found experimentally by Kloosterziel & van Heijst (1992), the decay of vortex velocities, and thus the circulation, is close to exponential for small Rossby numbers. This exponential decay is expected from linear Ekman dynamics, and has an associated timescale $T_E = H/(\nu\Omega)^{1/2}$, known as the Ekman timescale. In the experiments presented in this chapter, since for water at room temperature $\nu = 1.0 \times 10^{-6}$ m^2 s^{-1} the Ekman timescale is $T_E = 239$ s. The time evolution of the vortex circulation Γ can thus be described by

$$\Gamma(t) = \Gamma_0 \exp\left(-\frac{t}{T_E}\right), \tag{4.4}$$

with Γ_0 the initial circulation. The same exponential time dependence is true for the constant part of the shear strength, denoted by α_0. This constant shear also decays in time with an associated timescale T_E. The shear perturbation, however, is continuously forced. The amplitude of the perturbation remains the same throughout each experiment.

4.2 Dye experiments

Dye experiments were used to gain qualitative information about the flow. Fluorescent dye, fluorescein, was added near the top stagnation point. The dye is advected along the unstable manifold of this stagnation point. As such the unstable manifold was visualised, and recorded with the camera. A collection of snapshots from the recording of an experiment is given in figure 4.1.

In this experiment a volume $V = 905 \pm 5$ ml was syphoned through the tube, resulting in a vortex with initial circulation $\Gamma_0 = (6.3 \pm 0.2) \times 10^{-3}$ m^2 s^{-1} (equation (4.3)). The basic-state shear strength $\alpha_0 = 0.1$ s^{-1} due to the increase in angular velocity $\Delta\Omega = 0.05$ rad s^{-1}. The perturbation amplitude $\epsilon = 0.4$ and frequency $f_s = 0.1$ s^{-1}.

From the images in figure 4.1 the structure of the unstable manifolds is clearly visible. During one period of the perturbation the change in shape shows the fluid exchange mechanism of the turnstile. The shape of the manifold is again the same after one period, as expected. The lobes are elongated towards the top right and bottom left, along the unstable manifolds of the hyperbolic points. This was also evident from the numerical simulations.

The images are symmetrical with respect to the vortex centre. The axis through the vortex centre and both hyperbolic points is tilted in clockwise direction. According to theory, this axis should be perpendicular to the shear flow. This observation will be further addressed in section 4.3.

A numerical simulation was performed with exactly the parameters as prescribed in this laboratory experiment. The parameters were $\gamma_0 = 6.3 \times 10^{-3}$ m^2 s^{-1}, $\alpha_0 = 0.1$ s^{-1}, $f_s = 0.1$ s^{-1}, and $\epsilon = 0.4$. The contour was placed around the top stagnation point. Part of the evolution of this contour in time is shown in figure 4.2. The shapes of the contours resemble the dye lines from figure 4.1. However, the axis through the vortex centre and the stagnation points is now exactly vertical. No tilt of this axis occurs here due to the vorticity of the point vortex being concentrated in one point.

Given the overall similarities between figures 4.1 and 4.2, it can be concluded that the point-vortex model used in the numerical simulations is indeed a good approximation to these laboratory experiments with a sink vortex.

4.3 Particle tracking experiments

Particle tracking experiments are performed to gain quantitative information about the flow. The analysis involves the following steps.

A large amount of passive tracer particles (Optimage, diameter 250 μm) float at the water surface. They are transported along with the flow. The flow is monitored with an SMD 1M15 digital camera of resolution 1024 $\times$ 1024 pixels and frame rate 7.5 Hz. The acquired images are processed with a high-resolution particle velocimetry method (HPV). HPV combines two techniques: particle tracking velocimetry (PTV) and particle image velocimetry (PIV). In PTV, individual particles in one frame are matched with candidate particles in the next frame. PIV consists of determining the averaged displacement of particles in corresponding image segments of subsequent frames. HPV combines both methods in that the PIV estimate is used as input for the PTV processing. A more detailed description of the used HPV method can be found in Bastiaans *et al.* (2002) and references therein.

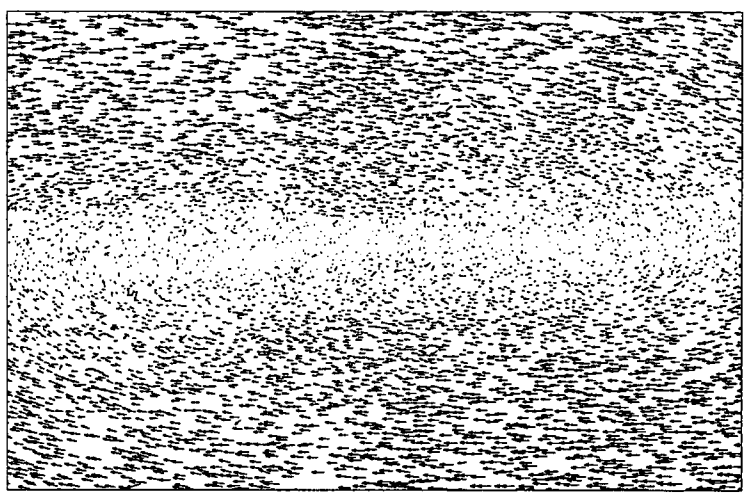

Figure 4.3: Example result from the HPV processing: an unstructured velocity field.

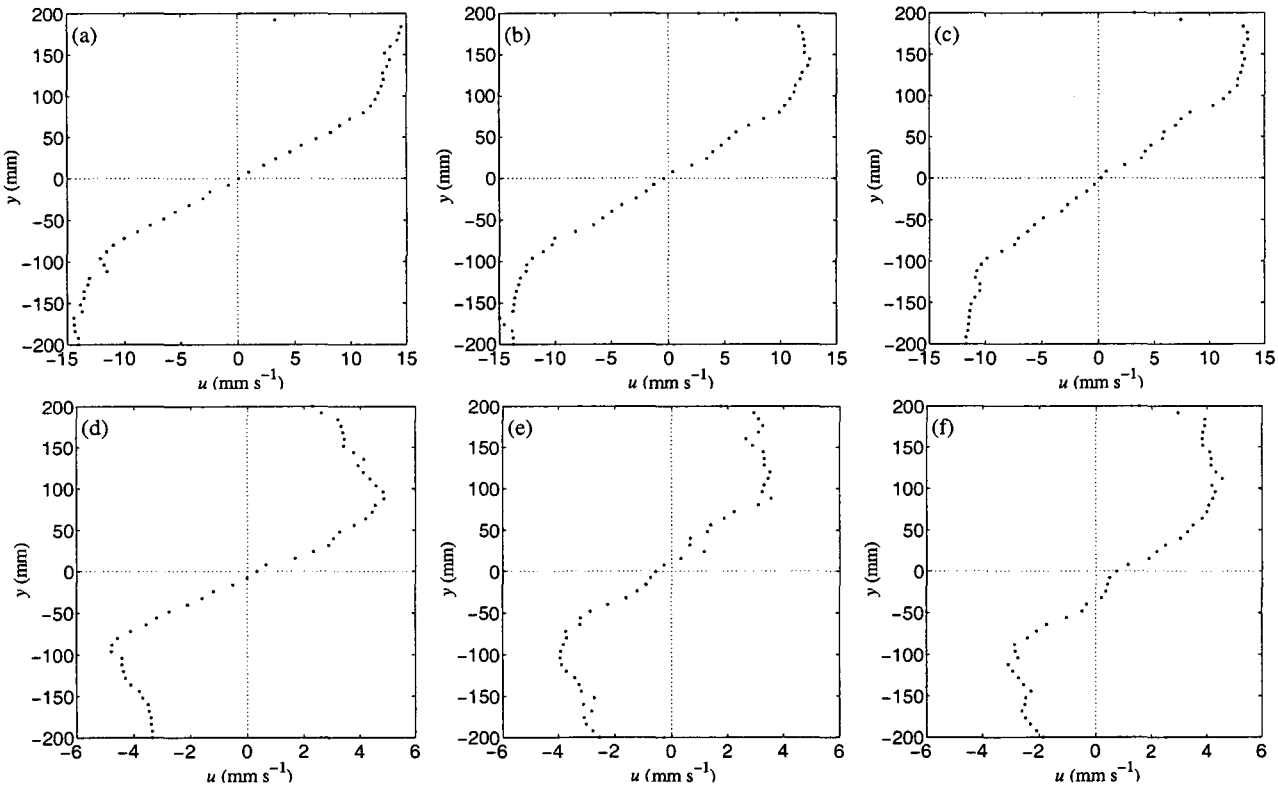

Figure 4.4: Profiles along $x = 0$ for the velocity component u in the x-direction. Graphs (a) at $t = 10$ s, (b) at $t = 40$ s, and (c) at $t = 70$ s are taken at times corresponding with a maximum in shear strength α. Graphs (d) at $t = 25$ s, (e) at $t = 55$ s, and (f) at $t = 85$ s are at a minimum of α.

Resulting from the HPV method is a collection of individual velocity vectors for selected times. An example result is shown in figure 4.3. These vectors are then interpolated on a regular grid using a Gaussian interpolation scheme. From this velocity distribution other quantities of interest (*e.g.* stream function, vorticity, etc.) can be computed.

Two different particle tracking experiments have been performed. In one experiment the shear flow has been investigated. In the other experiment the influence of the shear flow on a vortex has been monitored.

4.3.1 Shear flow

Important properties of the shear flow for the presented experiments are the linearity and the time dependence. These properties have been investigated with a particle tracking experiment. After an half-hour spin-up at 0.7 rad s^{-1} (at $t = 0$ s) the rotation velocity Ω was modulated as in equation (2.27), with $\Delta\Omega = 0.05$ rad s^{-1}, $\epsilon = 0.4$, and $f_s = \omega_s/2\pi = 0.1$ s^{-1}. The recordings were processed with the HPV software.

Velocity profiles through the centre of the tank at different times are shown in figure 4.4.

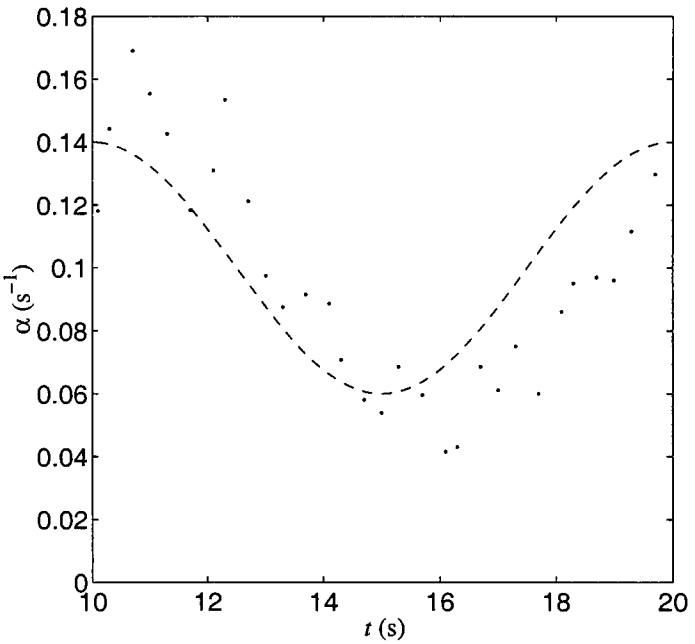

Figure 4.5: Time dependence of the shear strength α. The dots are the data points from the experiment. The dashed line depicts the theoretical prediction from equation (2.28) for $t \ll T_E$.

It is apparent that the shear flow is not linear across the tank. However, in the centre there is a region where an approximately linear shear is present. This region extends roughly from $y = -80$ to 80 mm. The velocity v in the y-direction is considerably smaller than u in this centre region (less than 0.5 mm s^{-1}). The rather violent forcing to generate the shear causes surface waves, and other effects near the tank walls. These influences distort the flow and cause the flow near the walls to deviate from a linear shear flow. The region of interest for the other experiments is the centre region, as the vortex is generated in the centre of the tank. Hence, the vortex will most likely not be influenced by these disturbing effects near the walls.

It is furthermore observable that the shear strength α gradually decreases with time. The decreasing slope indicates the decay of the shear flow. This is a manifestation of the Ekman decay.

The time dependence of the shear strength α is also further investigated. For one period of the perturbation (from $t = 10$ to 20 s) several velocity profiles were constructed, and the slope of the profile from $y = -80$ to 80 mm was determined using a least-squares method. The results are presented in figure 4.5. The large spread of the experimental data is an indication of a rather large experimental error. This is again caused by the vehement forcing and the accompanying surface waves. There is however still a trend visible. The harmonic variation is apparent. There is a lag in α of about 1 s with respect to the theoretical prediction. The extrema are also greater than is expected from theory.

The shear flow can be assumed linear in the centre region of the tank. There is an

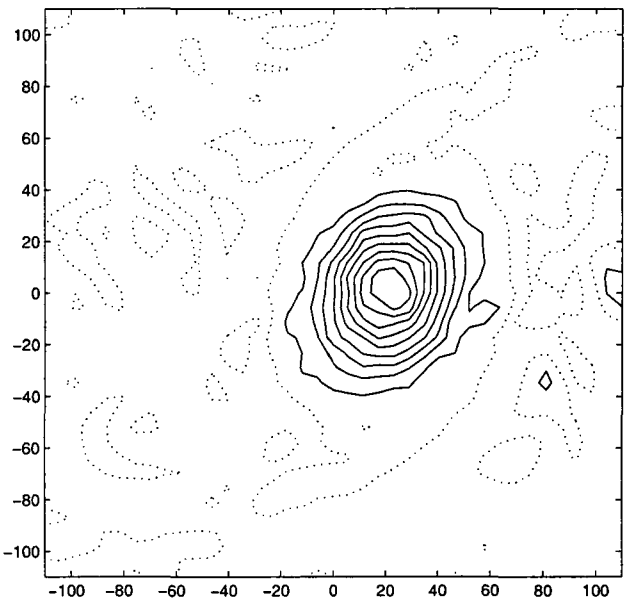

Figure 4.6: Vorticity contour plot at $t = 50$ s of the flow due to a vortex in a perturbed shear. The solid lines correspond to positive values of vorticity and the dotted lines to negative values of vorticity. The increment between contours is 0.2 s^{-1}. Values on the axes are in millimetres. The flow parameters are $\Gamma_0 = (6.3 \pm 0.2) \times 10^{-3}$ m^2 s^{-1}, $\Delta\Omega =$ 0.05 rad s^{-1}, $\epsilon = 0.4$, and $f_s = \omega_s/2\pi = 0.1$ s^{-1}.

approximately harmonic time dependence of the shear strength. The actual shear strength may vary considerably because of influences caused by the forcing.

4.3.2 Vortex in shear

In this particle tracking experiment a vortex was generated, which was then subjected to a perturbed shear. In this experiment the camera frame rate was 15 Hz. Water was syphoned through the perforated tube for 15 s. The volume of water withdrawn was $V = 900 \pm 5$ ml, resulting in a vortex with initial circulation $\Gamma_0 = (6.3 \pm 0.2) \times 10^{-3}$ m^2 s^{-1}. The syphoning ended 25 s before $t = 0$ s. Then, at $t = 0$ s, the rotation velocity Ω was modulated as in equation (2.27), with $\Delta\Omega = 0.05$ rad s^{-1}, $\epsilon = 0.4$, and $f_s = \omega_s/2\pi = 0.1$ s^{-1}. The recordings were again processed with the HPV software. From the obtained interpolated velocity vectors a vorticity distribution was calculated by finite-difference approximations.

An example vorticity distribution (for $t = 50$ s, corresponding to a maximum of the rotation velocity Ω) is depicted in figure 4.6. The vortex is visible as a slightly elliptic patch of positive vorticity. The long axis of the ellipse is not aligned with the y-axis, as was also noticed in the dye experiment in figure 4.1. This contrasts with the contour kinematics simulations with a point vortex. One cause of this difference is the vorticity having a continuous distribution instead of concentrated in a single point. The shape of the vorticity distribution can change due to the ambient flow, while the vorticity of a point

vortex always remains in the same point. The vorticity being spread out gives another cause for the different behaviour. Stripping of vorticity takes place at the extreme ends of the vortex. Vorticity is advected away from the vortex along the unstable manifolds, also decreasing its circulation in addition to Ekman decay and horizontal diffusion of vorticity. Vortex stripping of continuous vorticity patches in strain or shear is extensively investigated with numerical simulations by Dritschel (1989), Legras & Dritschel (1993), Legras & Dritschel (1994), and Mariotti *et al.* (1994).

The shear flow is apparent from the negative background vorticity present over the domain, as mentioned in section 2.2.2. The shear flow is manifested by a constant negative vorticity equal to the shear strength α over the entire tank.

In order to further investigate the stripping of vorticity, vorticity plots from one period of the perturbation are depicted in figure 4.7. The vorticity scale ranges from -0.2 s^{-1} (black) to 0.2 s^{-1} (white). Using this scale it is possible to discern the advection of vorticity in the lobes away from the vortex. The shapes of the gray areas at the extreme ends of the vortex match the shapes of the dye lines in figure 4.1. It can be observed that the lobe dynamics provide a mechanism for the advection of vorticity. The variation of the shear strength α is apparent from the greyscale level of the background. The dark background colour in figures 4.7a,f is a manifestation of the shear strength reaching its maximum value. A lighter background colour as in figures 4.7c,d indicates a smaller shear strength at those times.

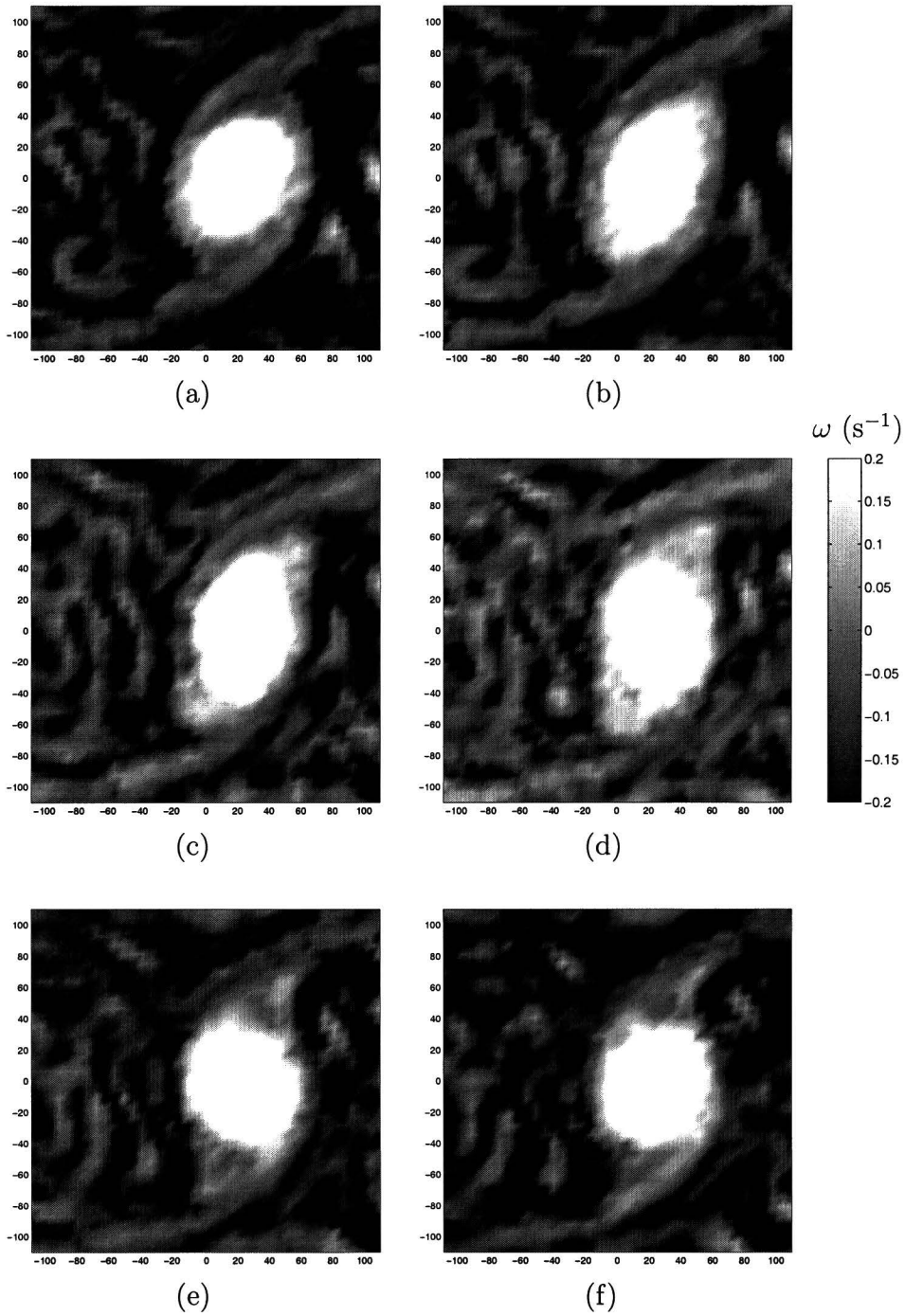

Figure 4.7: Vorticity plots of the flow due to a vortex in a perturbed shear. Plots (a) at $t = 50$ s and (f) at $t = 60$ s are at a maximum of the rotation velocity Ω. The images are shown at time intervals of 2 s. The vorticity range is limited to emphasise the vorticity filaments at the extreme ends of the vortex. The flow parameters are $\Gamma_0 = (6.3 \pm 0.2) \times 10^{-3}$ m^2 s^{-1}, $\Delta\Omega = 0.05$ rad s^{-1}, $\epsilon = 0.4$, and $f_s = \omega_s/2\pi = 0.1$ s^{-1}.

Chapter 5

Conclusions

The mixing properties of a point vortex in a harmonically perturbed linear shear flow have been investigated by numerical simulation. The unperturbed Hamiltonian system is fully integrable for all time. However, due to the presence of the perturbation chaotic particle paths are inevitable. The occurrence of chaotic particle paths results in complicated fluid mixing and transport properties of the system. Because of the chaotic behaviour it is not convenient to describe the flow by monitoring individual particle paths. Instead, concepts from dynamical systems theory are used.

There are two hyperbolic points present in the flow. Their associated stable and unstable manifolds organise the flow. In the Poincaré map these manifolds retain their shape, since each iteration of the Poincaré map occurs at the same phase of the perturbation. The intersections of the stable manifold of one hyperbolic point and the unstable manifold of the other hyperbolic point in the Poincaré map define enclosed areas, the so-called lobes. Fluid exchange between the region around the vortex and the exterior can be described in terms of these lobes. There are two entrainment lobes. Fluid inside one of the entrainment lobes at a certain time will be entrained in the vortex region in de following period of the perturbation. In the meantime, two detrainment lobes account in the same vein for the detrainment of fluid. The areas of the entrainment and detrainment lobes indicate the amount fluid exchange per cycle.

The manifolds are constructed with numerical simulations using the contour kinematics method. As the manifolds are known the lobes can be defined. Two methods to determine the lobe area have been used. The first method consists of direct numerical integration around the parts of the manifolds enclosing a lobe. The second method is to calculate the Melnikov function. The Melnikov function is an analytical expression that can be used to give an approximation of the lobe area for small perturbation amplitudes. A great advantage of the Melnikov function is that it only needs to be calculated once for a given geometry, while using the first method a new simulation has to be performed for each new set of parameters. The Melnikov approximation of the lobe area has a remarkably good correspondence to the result from the first method.

The notion of chaotic dynamics has been illustrated by further contour kinematics simulations. The contour exhibits stretching and folding while being advected by the flow.

In the Poincaré map Smale horseshoes are present, causing the stretching and folding. The existence of Smale horseshoes is evidence of chaotic dynamics. Another argument in favour of the chaotic dynamics is the length stretch of material elements. The length stretch is exponential for the flow under study. Exponential stretch is expected in chaotic dynamics, as opposed to linear stretch in the unperturbed flow. The length stretch increases faster for higher perturbation frequencies, since the contour is folded more often in that case.

A further variation on the contour kinematics simulations includes perturbation of the vortex strength instead of the shear strength in a simulation. The lobe area does not change in this case. There is only a half-period phase shift with respect to the former case.

Also the influence of exponential vortex decay has been investigated. The vortex decays due to Ekman suction, diffusion of vorticity, and vortex stripping. To simulate the decay, the point vortex strength was decreased exponentially in some contour kinematics simulations. No fundamentally different behaviour from the non-decaying simulations was found as long as the e-folding timescale was not too small.

An alternative method to investigate the fluid transport is to monitor the advection of a large amount of passive markers. The entrainment lobes are filled with markers on a regular grid. The particles will be transported to the interior region during the next cycle of the perturbation. Then the position of each marker after each iteration of the Poincaré map is recorded. The escape time of each marker can now be defined as the cycle during which the marker is transported to the exterior flow. As such an escape time distribution is obtained. The escape time distribution gives the number of particles that escapes during each cycle. A related quantity is the escape area distribution, which can be interpreted as the number of particles that has escaped the interior region up to a given cycle. Both distributions can be split into two parts. Since the system contains two detrainment lobes transport takes place in two directions. The escape time and escape area distributions that have been determined show that the time of residence in the interior region for markers is larger for higher perturbation frequency. There is also a paradoxical behaviour with respect to the direction of the transport. Fluid entrained from one side of the vortex is more likely to be detrained after almost a full revolution around the vortex. This is due to the lobe dynamics. The detrainment lobe transporting fluid to the far side is encountered first during the revolution around the vortex.

The data from these simulations can also be visualised in another way to gain additional insights. Since the times at which the data were recorded all correspond to the same phase of the perturbation they form a Poincaré section. From the Poincaré section regions can be recognised that do not participate in the mixing. These regions are never penetrated by particles emanating from the entrainment lobe. The section around the vortex is an example. There are closed elliptic particle trajectories around the vortex position that are largely unaffected by the perturbation. In some cases other blank regions appeared as well. To further investigate those subregions, markers were placed inside these regions. Simulation of the advection of these markers showed that the markers move from subregion to subregion while rotating around the vortex section. These subregions are known as resonance bands or stochastic layers. The number of subregions found increased with increasing perturbation frequency. The remaining area of the interior region, *i.e.* the parts

that have been reached by markers, is known as the mixing region. There appears to be a maximum size of the mixing region, and an associated perturbation frequency. The size of the mixing region decreases if the perturbation frequency is increased. The same is true for lower perturbation frequencies than this value.

Laboratory experiments have been performed in an attempt to visualise the manifolds in a real flow. These experiments were carried out in a tank mounted on a rotating table, to obtain a quasi-two-dimensional flow. A linear shear flow with a time-periodic perturbation was generated by a variation of the rotation velocity. By syphoning water through a perforated tube a vortex was generated. The unstable manifolds were visualised by inserting dye into the flow near one of the two stagnation points. The manifold geometry observed here matched the geometry from a contour kinematics simulation remarkably well. It is striking that the results from experiment and simulation are so alike since a point vortex is only a very crude approximation of a laboratory vortex with a spatial vorticity distribution.

Another way of monitoring the flow in a laboratory experiment is with high-resolution particle velocimetry. Subsequent images of a large number of passive tracer particles floating at the water surface are analysed digitally to determine the particle paths, and hence the velocity vectors. The velocity vectors can then be interpolated on a rectangular grid, to calculate other quantities such as vorticity. Two particle tracking experiments have been performed. In one experiment the linearity and time dependence of the shear flow was investigated. In the centre region of the the tank the shear flow was found to be reasonably linear. Closer to the edges there was no linear shear flow. The vehement forcing caused rather large disturbances near the tank walls. The time dependence was also found to be approximately harmonic, be it with a large spread in the data points. This is again due to the forcing and associated disturbances. In the other experiment the vorticity distribution of a vortex was monitored while being subjected to the perturbed shear flow. It was observed that the lobe dynamics provide a mechanism for advection of vorticity away from the vortex. The shapes of the lobes as found in the images of the dye experiment matched the shapes as found in the vorticity plots.

Emanating from this work there are some suggestions for further research on this subject, both numerically and experimentally. In some numerical simulations an interesting subdivision of the vortex region was observed. Resonance bands were present, with related barriers to transport. A more detailed study of the structure of this region is possible with advection simulations at higher resolution and with more markers. In the laboratory experiments the upper limits of the current set-up were reached with regard to the perturbation frequency. A turntable with a more powerful forcing may allow for higher perturbation frequencies. A larger-scale set-up can be used to perform particle tracking experiments at a higher resolution, to investigate the vorticity distribution in more detail.

Bibliography

[1] AREF, H. (1984) Stirring by chaotic advection. *J. Fluid Mech.* **143**, 1–21.

[2] ARNOL'D, V.I. & AVEZ, A. (1968) *Ergodic Problems of Classical Mechanics.* W.A. Benjamin.

[3] BASTIAANS, R.J.M., PLAS, G.A.J. VAN DER & KIEFT, R.N. (2002) The performance of a new PTV algorithm applied in super-resolution PIV. *Exp. Fluids* **32**, 346–356.

[4] BEIGIE, D., LEONARD, A. & WIGGINS, S. (1994) Invariant manifold templates for chaotic advection. *Chaos, Solitons & Fractals* **4**, 749–868.

[5] COUDER, Y. & BASDEVANT, B. (1986) Experimental and numerical study of vortex couples in two-dimensional flows. *J. Fluid Mech.* **173**, 225–251.

[6] CREMERS, B.E. (1993) Chaotic advection by dipolar vortices on topographic β-plane. Master's report R-1211-A, Eindhoven University of Technology, The Netherlands.

[7] DRITSCHEL, D.G. (1989) Strain-induced vortex stripping. In *Mathematical Aspects of Vortex Dynamics.* (ed. R.E. Caflisch), pp. 107–119. Society of Industrial and Applied Mathematics.

[8] FLÓR, J.B. & HEIJST, G.J.F. VAN (1996) Stable and unstable monopolar vortices in a stratified fluid. *J. Fluid Mech.* **311**, 257–287.

[9] GUCKENHEIMER, J. & HOLMES, P. (1983) *Nonlinear Oscillations, Dynamical Systems and Bifurcations of Vector Fields.* Springer.

[10] HEIJST, G.J.F. VAN, DAVIES, P.A. & DAVIS, R.G. (1990) Spin-up in a rectangular container. *Phys. Fluids A* **2**, 150–159.

[11] HOPFINGER, E.J. & HEIJST, G.J.F. VAN (1993) Vortices in rotating fluids. *Annu. Rev. Fluid Mech.* **25**, 241–289.

[12] KIDA, S. (1981) Motion of an elliptic vortex in a uniform shear flow. *J. Phys. Soc. Japan* **50**, 3517–3520.

[13] KLOOSTERZIEL, R.C. & HEIJST, G.J.F. VAN (1992) The evolution of stable barotropic vortices in a rotating free-surface fluid. *J. Fluid Mech.* **239**, 607–629.

[14] KUNDU, P.K. (1990) *Fluid Mechanics.* Academic Press.

[15] LEGRAS, B., SANTANGELO, P. & BENZI, R. (1988) High-resolution numerical experiments for forced two-dimensional turbulence. *Europhys. Lett.* **3**, 811–818.

[16] LEGRAS, B. & DRITSCHEL, D.G. (1993) Vortex stripping and the generation of high vorticity gradients in two-dimensional flows. *Appl. Sci. Res.* **51**, 445–455.

[17] LEGRAS, B. & DRITSCHEL, D.G. (1994) Vortex stripping. In *Modelling of Oceanic Vortices.* (ed. G.J.F. van Heijst), pp. 51–59. North Holland.

[18] LEONARD, A., ROM-KEDAR, V. & WIGGINS, S. (1987) Fluid mixing and dynamical systems. *Nuclear Physics B* (Proc. Suppl.) **2**, 179–190.

[19] LIPZIG, N.P.M. VAN (1994) Chaotisch transport door een tripolaire wervel op een γ-vlak. Master's report R-1277-A, Eindhoven University of Technology, The Netherlands.

[20] MARIOTTI, A., LEGRAS, B. & DRITSCHEL, D.G. (1994) Vortex stripping and the erosion of coherent structures in two-dimensional flows. *Phys. Fluids* **6**, 3944–3962.

[21] MELESHKO, V.V. & HEIJST, G.J.F. VAN (1994) Interacting two-dimensional vortex structures: point vortices, contour kinematics and stirring properties. *Chaos, Solitons & Fractals* **4**, 977–1010.

[22] MELNIKOV, V.K. (1963) On the stability of the center for time periodic perturbations. *Trans. Moscow Math. Soc.* **12**, 1–57.

[23] MOORE, D.W. & SAFFMAN, P.G. (1971) Structure of a line vortex in an imposed strain. In *Aircraft Wake Turbulence and its Detection.* (ed. J.H. Olsen, A. Goldburg & M. Rogers), pp. 339–354.

[24] OTTINO, J.M. (1989) *The Kinematics of Mixing: Stretching, Chaos and Transport.* Cambridge University Press.

[25] ROM-KEDAR, V., LEONARD, A. & WIGGINS, S. (1990) An analytical study of transport, mixing and chaos in an unsteady vortical flow. *J. Fluid Mech.* **214**, 347–394.

[26] PEDLOSKY, J. (1979) *Geophysical Fluid Dynamics.* Springer.

[27] ROM-KEDAR, V. & WIGGINS, S. (1991) Transport in two-dimensional maps: Concepts, examples, and a comparison of the theory of Rom-Kedar and Wiggins with the Markov model of MacKay, Meiss, Ott, and Percival. *Physica D* **51**, 248–266.

[28] TRIELING, R.R., BECKERS, M. & HEIJST, G.J.F. VAN (1997) Dynamics of monopolar vortices in a strain flow. *J. Fluid Mech.* **345**, 165–201.

[29] TRIELING, R.R. & HEIJST, G.J.F. VAN (1998) Kinematic properties of monopolar vortices in a strain flow. *Fluid Dyn. Res.* **23**, 319–341.

[30] VELASCO FUENTES, O.U., HEIJST, G.J.F. VAN & CREMERS, B.E. (1995) Chaotic transport by dipolar vortices on a β-plane. *J. Fluid Mech.* **291**, 139–161.

[31] VELASCO FUENTES, O.U., HEIJST, G.J.F. VAN & LIPZIG, N.P.M. VAN (1996) Unsteady behaviour of a topography-modulated tripole. *J. Fluid Mech.* **307**, 11–41.

[32] WIGGINS, S. (1988) *Global Bifurcations and Chaos — Analytical Methods.* Springer.

[33] WIGGINS, S. (1992) *Chaotic Transport in Dynamical Systems.* Springer.

Appendix A

Parametrisation of the unperturbed manifold

The stream function for the unperturbed flow due to a point vortex in a linear shear flow is (2.2)

$$\Psi = \frac{1}{2}\alpha y^2 - \frac{\gamma}{4\pi}\ln(x^2+y^2) + c. \tag{A.1}$$

The two stagnation points of the flow are given by

$$(x,y) = (0,\pm r_s) = \left(0, \pm\sqrt{\frac{\gamma}{2\pi\alpha}}\right). \tag{A.2}$$

By evaluating the stream function in one of the stagnation points the equation for the separatrix is obtained

$$x = \pm\sqrt{r_s^2 \exp\left(\frac{y^2}{r_s^2} - 1\right) - y^2}, \tag{A.3}$$

where the plus sign is for Ψ_e and the minus sign for Ψ_w (figure 2.1). The advection equations are

$$\begin{aligned} \frac{dx}{dt} &= \frac{\partial\Psi}{\partial y} = \alpha y - \frac{\gamma}{2\pi}\frac{y}{x^2+y^2}, \\ \frac{dy}{dt} &= -\frac{\partial\Psi}{\partial x} = \frac{\gamma}{2\pi}\frac{x}{x^2+y^2}. \end{aligned} \tag{A.4}$$

Then use (A.3) in (A.4) to obtain for dy/dt:

$$\frac{dy}{dt} = \pm\frac{\gamma}{2\pi}\frac{\sqrt{r_s^2\exp\left(\frac{y^2}{r_s^2}-1\right) - y^2}}{r_s^2\exp\left(\frac{y^2}{r_s^2}-1\right)}. \tag{A.5}$$

The parametrisation of the separatrix is given by

$$\int_0^t d\tilde{t} = \pm\frac{2\pi}{\gamma}\int_0^{y(t)} \frac{r_s^2 \exp\left(\frac{\tilde{y}^2}{r_s^2} - 1\right)}{\sqrt{r_s^2 \exp\left(\frac{\tilde{y}^2}{r_s^2} - 1\right) - \tilde{y}^2}} d\tilde{y}, \tag{A.6}$$

which can be used to calculate $y(t)$ for all t. $y(0)$ is defined to be 0. If $y(t)$ is known, $x(t)$ can be computed from (A.3). Thus the full parametrisation $(x(t), y(t))$ is obtained.

Appendix B

Derivation of the Melnikov function

The stream function for the flow due to a point vortex in a perturbed linear shear flow is

$$\Psi = \frac{1}{2}\alpha_0[1 + \epsilon\cos(\omega_s t)]y^2 - \frac{\gamma}{4\pi}\ln(x^2 + y^2) + c, \tag{B.1}$$

where ϵ is the amplitude of perturbation, and ω_s the frequency of perturbation. The following advection equations result from this stream function

$$\begin{aligned} \frac{dx}{dt} &= \alpha_0[1 + \epsilon\cos(\omega_s t)]y - \frac{\gamma}{2\pi}\frac{y}{x^2 + y^2}, \\ \frac{dy}{dt} &= \frac{\gamma}{2\pi}\frac{x}{x^2 + y^2}. \end{aligned} \tag{B.2}$$

From (2.10), the functions f_i and g_i are

$$\begin{aligned} f_1 &= \alpha_0 y - \frac{\gamma}{2\pi}\frac{y}{x^2 + y^2}, \\ f_2 &= \frac{\gamma}{2\pi}\frac{x}{x^2 + y^2}, \\ g_1 &= \alpha_0 y\cos(\omega_s t), \\ g_2 &= 0. \end{aligned} \tag{B.3}$$

The Melnikov function (2.15) is then

$$\begin{aligned} M(t_0) &= -\frac{\gamma\alpha_0}{2\pi}\int_{-\infty}^{\infty}\frac{xy}{x^2 + y^2}\cos[\omega_s(t + t_0)]dt \\ &= -\frac{\gamma\alpha_0}{2\pi}\int_{-\infty}^{\infty}\frac{xy}{x^2 + y^2}[\cos(\omega_s t)\cos(\omega_s t_0) - \sin(\omega_s t)\sin(\omega_s t_0)]dt \\ &= \frac{\gamma\alpha_0}{\pi}\sin(\omega_s t_0)\int_0^{\infty}\frac{xy}{x^2 + y^2}\sin(\omega_s t)dt. \end{aligned} \tag{B.4}$$

The last step comes from the fact that x is an odd function of time, while y is even in time. So only the sine part contributes to the integral. Now use the equation for the

separatrix (A.3). The equation for Ψ_e is used. By symmety the result is also valid for Ψ_w. Now equation (B.4) can be written as

$$M(t_0) = \frac{\gamma\alpha_0}{\pi}\sin(\omega_s t)\int_0^\infty \frac{y\sqrt{r_s^2\exp\left(\frac{y^2}{r_s^2}-1\right)-y^2}}{r_s^2\exp\left(\frac{y^2}{r_s^2}-1\right)}\sin(\omega_s t)dt. \tag{B.5}$$

Now rewrite the integral over t to an integral over y with the parametrisation (A.6) of the separatrix

$$\int_0^\infty dt \rightarrow \int_0^{r_s}\frac{2\pi}{\gamma}\frac{r_s^2\exp\left(\frac{\tilde{y}^2}{r_s^2}-1\right)}{\sqrt{r_s^2\exp\left(\frac{\tilde{y}^2}{r_s^2}-1\right)-\tilde{y}^2}}d\tilde{y}, \tag{B.6}$$

and define the function $f(\xi)$ as

$$f(\xi) = \int_0^\xi \frac{2\pi}{\gamma}\frac{r_s^2\exp\left(\frac{\tilde{y}^2}{r_s^2}-1\right)}{\sqrt{r_s^2\exp\left(\frac{\tilde{y}^2}{r_s^2}-1\right)-\tilde{y}^2}}d\tilde{y}. \tag{B.7}$$

This leaves for $M(t_0)$

$$M(t_0) = 2\alpha_0\sin(\omega_s t_0)\int_0^{r_s} y\sin[\omega_s f(y)]dy. \tag{B.8}$$

Finally, substituting $\zeta = y^2/r_s^2$ and $p = \omega_s/2\alpha_0$ gives

$$M(t_0) = \frac{\gamma}{2\pi}P(p)\sin(\omega_s t_0), \tag{B.9}$$

with

$$P(p) = \int_0^1 \sin[pf(\zeta)]d\zeta. \tag{B.10}$$

The function $P(p)$ can be evaluated numerically, and is shown in figure 3.3.

Another interesting case is to perturb the vortex strength γ instead of the shear strength α

$$\gamma(t) = \gamma_0[1+\epsilon\cos(\omega_s t)]. \tag{B.11}$$

Now the advection equations are

$$\begin{aligned}\frac{dx}{dt} &= \alpha y - \frac{\gamma_0}{2\pi}\frac{y}{x^2+y^2} - \epsilon\frac{\gamma_0}{2\pi}\frac{y}{x^2+y^2}\cos(\omega_s t),\\ \frac{dy}{dt} &= \frac{\gamma_0}{2\pi}\frac{x}{x^2+y^2} + \epsilon\frac{\gamma_0}{2\pi}\frac{x}{x^2+y^2}\cos(\omega_s t).\end{aligned} \tag{B.12}$$

In this case the functions f_i and g_i are

$$\begin{aligned} f_1 &= \alpha y - \frac{\gamma_0}{2\pi}\frac{y}{x^2+y^2}, \\ f_2 &= \frac{\gamma_0}{2\pi}\frac{x}{x^2+y^2}, \\ g_1 &= -\frac{\gamma_0}{2\pi}\frac{y}{x^2+y^2}\cos(\omega_s t), \\ g_2 &= \frac{\gamma_0}{2\pi}\frac{x}{x^2+y^2}\cos(\omega_s t). \end{aligned} \tag{B.13}$$

Inserting these functions into equation (2.15) gives the same result as in the case of perturbed shear, except for a change of sign

$$M(t_0) = -\frac{\gamma_0}{2\pi}P(p)\sin(\omega_s t_0). \tag{B.14}$$

The change of sign corresponds to a half-period phase shift between the two cases. Both lead to the same rate of fluid exchange, and they differ only by a phase factor.

Appendix C

Exponential stretch near $\mathbf{p}_+$

Consider the unperturbed flow near the hyperbolic point $\mathbf{p}_+$. A passive contour placed around $\mathbf{p}_+$ will be exponentially stretched in one direction, and exponentially contracted in another. The stretch can be understood as follows. Near $\mathbf{p}_+$, define a local y-coordinate $\tilde{y} = y - r_s$. The advection equations are

$$\begin{aligned} \frac{dx}{dt} &= \alpha(r_s + \tilde{y}) - \frac{\gamma}{2\pi} \frac{r_s + \tilde{y}}{x^2 + (r_s + \tilde{y})^2}, \\ \frac{d\tilde{y}}{dt} &= \frac{\gamma}{2\pi} \frac{x}{x^2 + (r_s + \tilde{y})^2}. \end{aligned} \tag{C.1}$$

In a local first-order Taylor expansion in x and $\tilde{y}$ this reduces to

$$\begin{aligned} \frac{dx}{dt} &= \alpha(r_s + \tilde{y}) - \frac{\gamma}{2\pi} \left(\frac{1}{r_s} - \frac{1}{r_s^2} \tilde{y} \right) = 2\alpha\tilde{y}, \\ \frac{d\tilde{y}}{dt} &= \frac{\gamma}{2\pi} \frac{1}{r_s^2} x = \alpha x. \end{aligned} \tag{C.2}$$

Scale $\tilde{y}$ by $\sqrt{2}$: $y^* = \sqrt{2}\tilde{y}$

$$\begin{aligned} \frac{dx}{dt} &= \sqrt{2}\alpha y^*, \\ \frac{dy^*}{dt} &= \sqrt{2}\alpha x. \end{aligned} \tag{C.3}$$

The solution to this system of coupled differential equations is given by

$$\begin{aligned} x(t) &= A \exp(\sqrt{2}\alpha t) + B \exp(-\sqrt{2}\alpha t), \\ y^*(t) &= A \exp(\sqrt{2}\alpha t) - B \exp(-\sqrt{2}\alpha t). \end{aligned} \tag{C.4}$$

To interpret the solution, introduce new coordinates $\xi = x + y^*$, $\eta = y^* - x$:

$$\begin{aligned} \xi &= 2A \exp(\sqrt{2}\alpha t), \\ \eta &= -2B \exp(\sqrt{2}\alpha t). \end{aligned} \tag{C.5}$$

From equation (C.5) it is clear that there is exponential stretch in the direction of ξ, and exponential contraction in the direction of η. By incompressibility the area enclosed by a contour must be preserved. Therefore A and B must be of equal magnitude.

Going back to the local coordinates x and $\tilde{y}$, the result is an exponentially expanding term $\sim \exp(\sqrt{2}\alpha t)$ along the line $\tilde{y} = \frac{1}{2}\sqrt{2}x$ and an exponentially diminishing term $\sim \exp(-\sqrt{2}\alpha t)$ along the line $\tilde{y} = -\frac{1}{2}\sqrt{2}x$. There is exponential stretching or exponential contraction along the directions $\tilde{y} = \pm\frac{1}{2}\sqrt{2}x$, the tangent lines of the separatrix in $\mathbf{p}_+$.

Appendix D

Geometry of lobe intersections

The geometries of the lobe intersections $E \cap F^{-k+1}D$ for the particle transport simulations are shown in figures D.1 and D.2, for selected values of k. In figure D.1 the intersections for the simulation with perturbation frequency $\omega_s = 0.4\pi$ are depicted, while figure D.2 contains the intersections for the simulation with perturbation frequency $\omega_s = 1.6\pi$. The results for the other simulation, with $\omega_s = 0.8\pi$, are shown in figure 3.14.

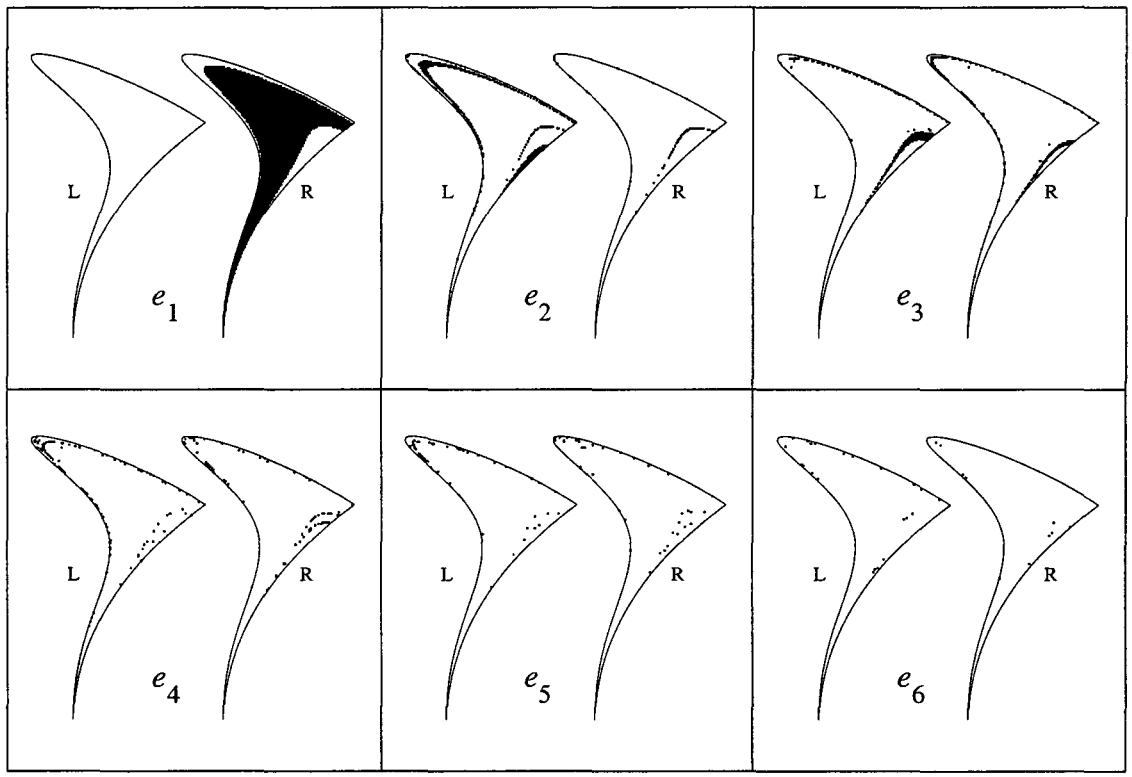

Figure D.1: Geometry of $E \cap F^{-k+1}D$ for several values of k. 'L' stands for the intersection of E with the detrainment lobe transporting fluid to the left, 'R' is the intersection of E with the detrainment lobe transporting fluid to the right. Perturbation frequency $\omega_s = 0.4\pi$.

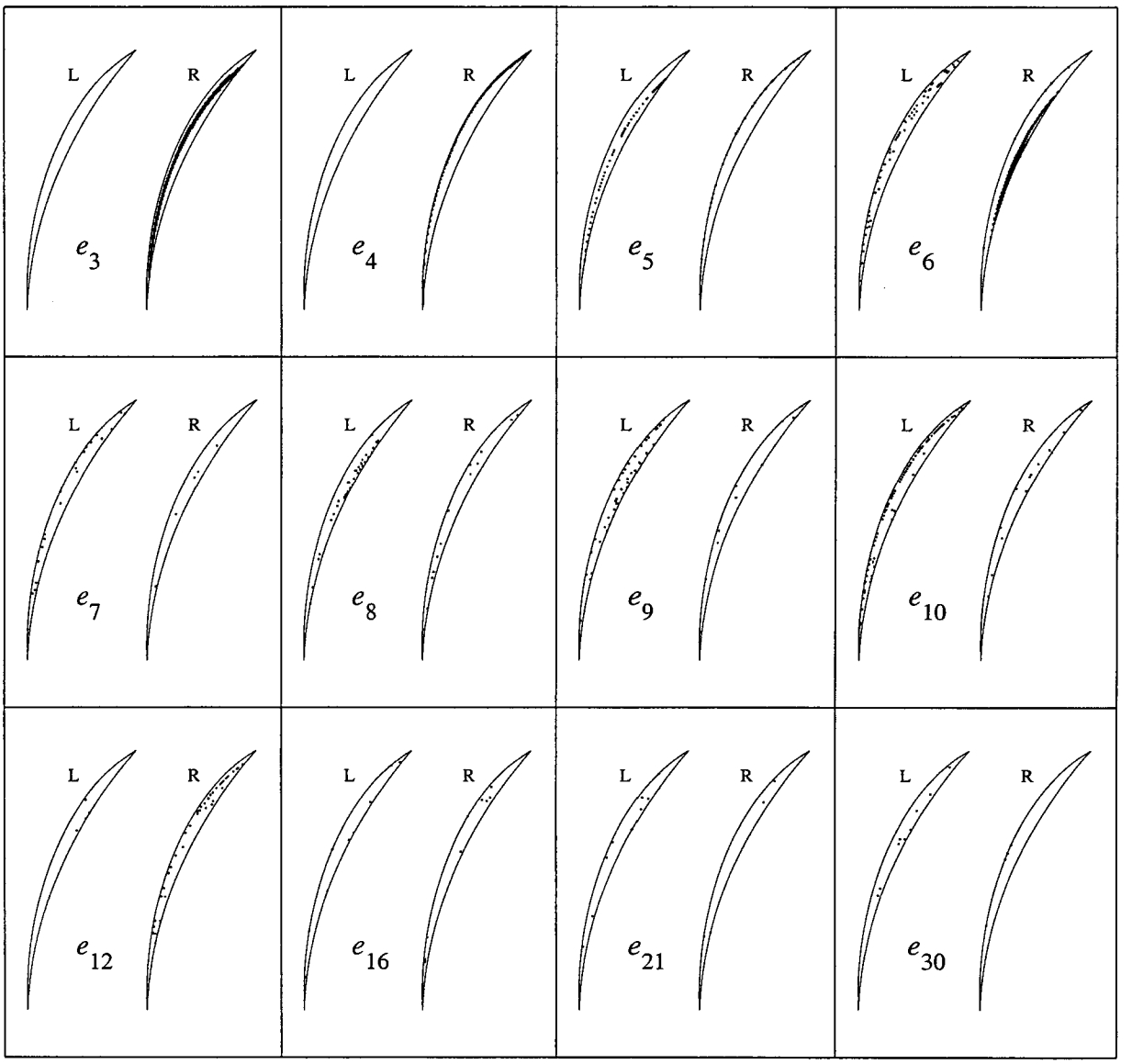

Figure D.2: Geometry of $E \cap F^{-k+1} D$ for several values of k. 'L' stands for the intersection of E with the detrainment lobe transporting fluid to the left, 'R' is the intersection of E with the detrainment lobe transporting fluid to the right. Perturbation frequency $\omega_s = 1.6\pi$.

Appendix E

Poincaré sections

The Poincaré section for the particle transport simulation with perturbation frequency $\omega_s = 0.8\pi$ is given in figure E.1. $N = 7808$ particles were initially placed in entrainment lobe E on a grid with mesh 0.01. Another Poincaré section is depicted in figure E.2, for $\omega_s = 0.4\pi$. $N = 4741$ particles were initially place in lobe E on a grid with mesh 0.02.

In figures E.3 and E.4, two more Poincaré sections are shown to further illustrate the emerging resonance bands. Figure E.3 shows the evolution of $N = 3202$ particles, initially placed in E on a grid with mesh 0.005 for $\omega_s = 2\pi$. In figure E.4 $N = 2752$ particles are placed in E on a grid with mesh 0.002 for $\omega_s = 3.2\pi$.

In all figures in this appendix all points are also mirrored in the origin to account for the other entrainment lobe.

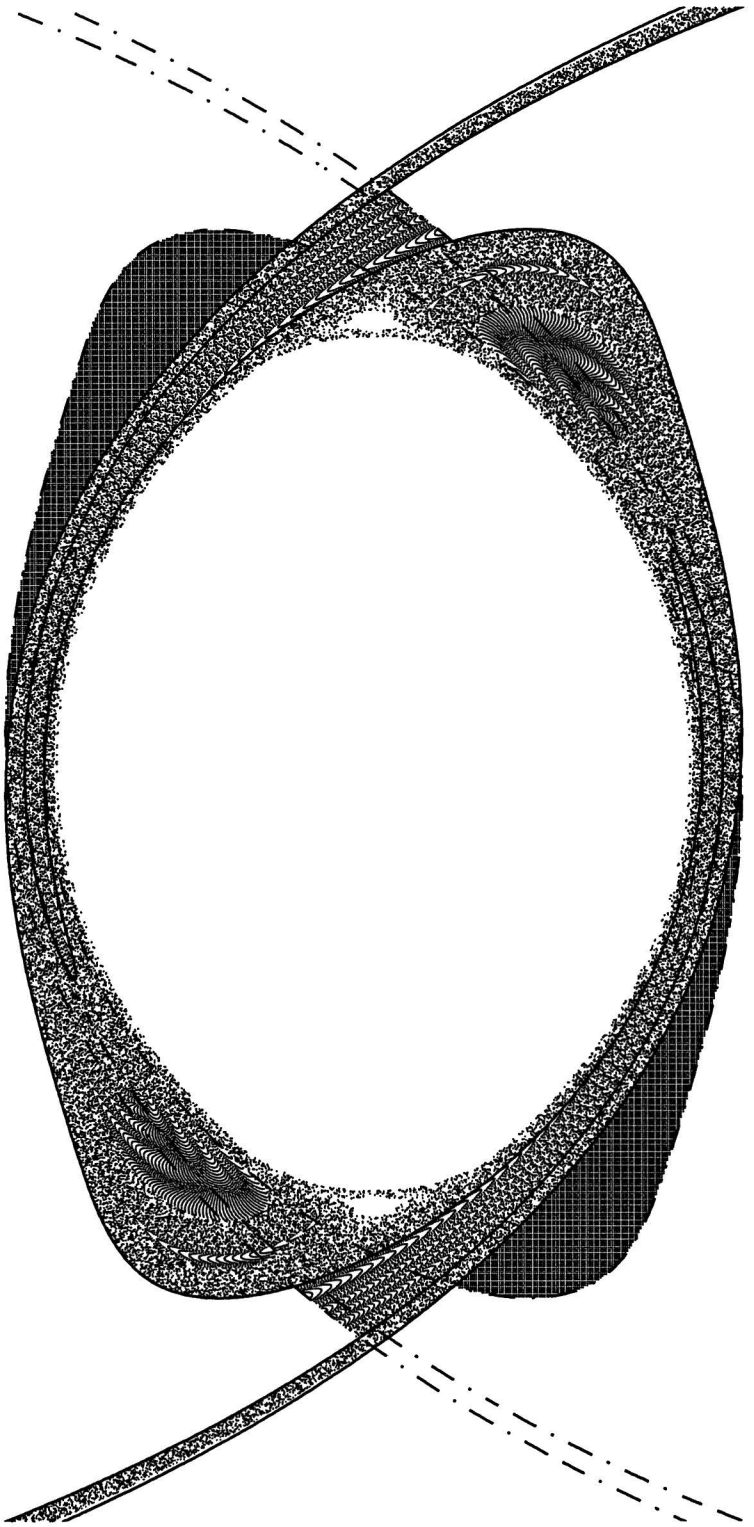

Figure E.1: Poincaré section after 50 cycles of 2×7808 *particles initially in the entrainment lobes on a grid of mesh 0.01. The unstable manifolds are depicted with solid lines. The stable manifolds are shown with dash-dotted lines. Perturbation frequency* $\omega_s = 0.8\pi$.

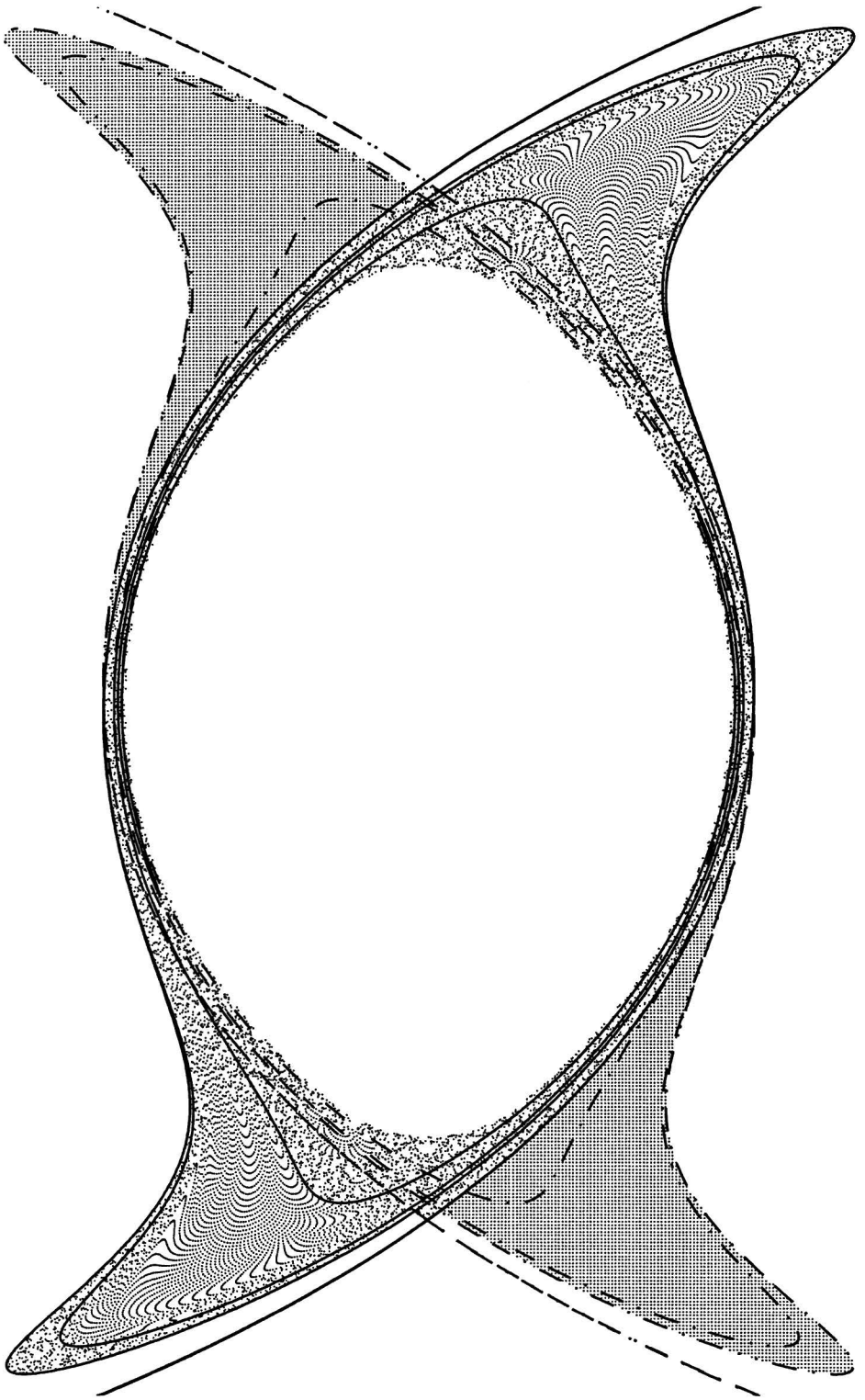

Figure E.2: Poincaré section after 50 cycles of 2×4741 *particles initially in the entrainment lobes on a grid of mesh 0.02. The unstable manifolds are depicted with solid lines. The stable manifolds are shown with dash-dotted lines. Perturbation frequency* $\omega_s = 0.4\pi$.

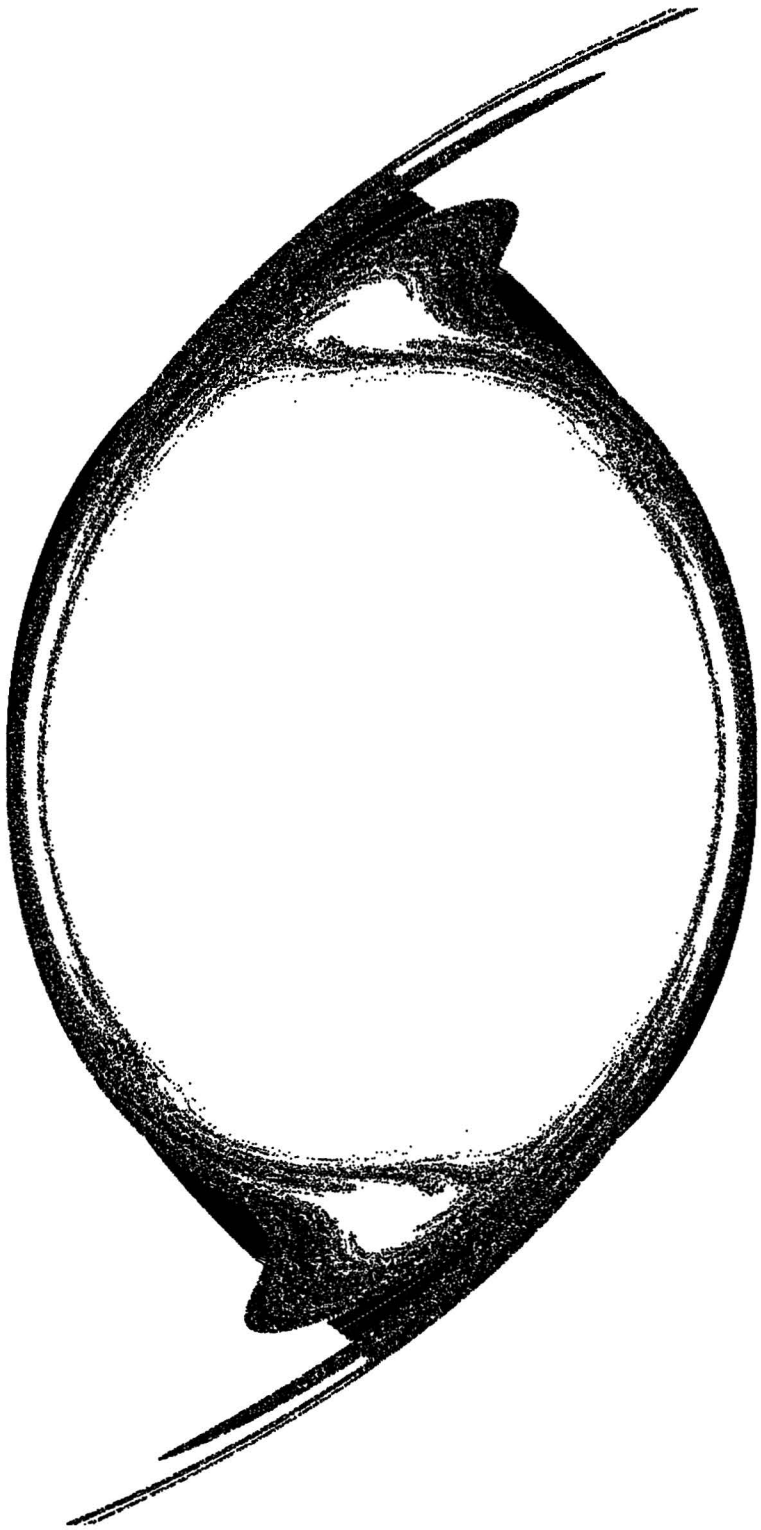

Figure E.3: Poincaré section after 50 cycles of 2×3202 *particles initially in the entrainment lobes on a grid of mesh 0.005. The manifolds are left out. The* $p : q = 4 : 1$ *resonance band is visible as the four blank regions around the blank vortex region. Perturbation frequency* $\omega_s = 2\pi$.

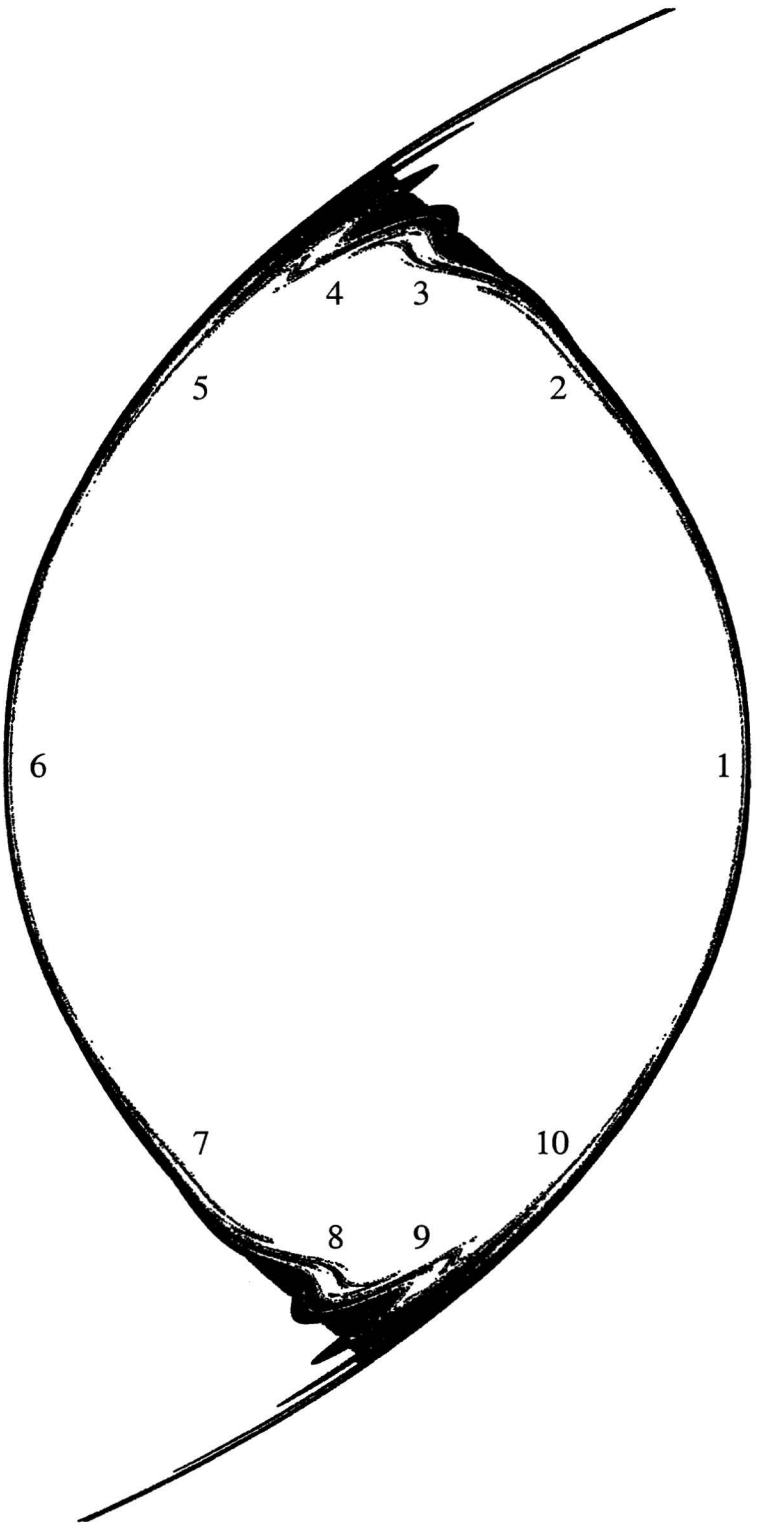

Figure E.4: Poincaré section after 50 cycles of 2×2752 *particles initially in the entrainment lobes on a grid of mesh 0.002. The manifolds are left out. The* $p : q = 10 : 1$ *resonance band is visible as the ten small blank regions around the blank vortex region. Perturbation frequency* $\omega_s = 3.2\pi$.

Appendix F

Technology assessment

The relevance of the study of the time-perturbed shear-vortex flow is twofold. It has applications in the research of two-dimensional turbulence, as well as in the study of stirring and mixing.

Two-dimensional flows are common in the fluid layers covering the Earth: both atmospheric and oceanic flows are to good approximation two-dimensional. The study of two-dimensional turbulence aids in understanding these flows. The oceans play an important role in large-scale heat and biomass transport. The knowledge of oceanic and atmospheric dynamics (geophysical fluid dynamics) provides tools to construct climate models. A better understanding of geophysical fluid dynamics is useful for predicting tomorrow's weather and even the long-term evolution of our climate.

Stirring and mixing are complex phenomena that are of paramount importance to industry. Improving the mixing of reactants can greatly increase the efficiency of chemical reactions, by increasing the contact surface. Effective stirring also enhances processes in which substances need to be dissolved. The production efficiency can be increased by application of efficient stirring and mixing.